ELECTRIC ARC CHARACTERISATION AND FURNACE PROCESS MONITORING WITH OPTICAL EMISSION SPECTROSCOPY AND IMAGE ANALYSIS

HENRI PAUNA

University of Oulu Graduate School
University of Oulu
Faculty of Technology
Process Metallurgy Research Unit

Academic dissertation to be presented with the assent of the Doctoral Training Committee of Technology and Natural Sciences of the University of Oulu for public discussion in the Auditorium L5, on October 30th, 2020, at 12 o'clock noon.

REPORT SERIES IN PHYSICAL SCIENCES Report No. 136
OULU 2020 • UNIVERSITY OF OULU

Opponent
Associate professor Valentina Colla, Sant'Anna School of Advanced Studies, Italy

Reviewers
Professor Jianhua Liu, University of Science and Technology Beijing, China
Associate professor Anders Tilliander, KTH Royal Institute of Technology, Sweden

Custos
Professor Timo Fabritius, University of Oulu, Finland

Supervisors
Professor Timo Fabritius, University of Oulu, Finland
Professor Marko Huttula, University of Oulu, Finland
Doctor Matti Aula, University of Oulu, Finland

ISBN 978-952-62-2730-6 (print)
ISBN 978-952-62-2731-3 (electronic)
ISSN 1239-4327
PunaMusta Oy (Yliopistopaino)
Oulu 2020

Pauna, Henri Tapani: Electric arc characterisation and furnace process monitoring with optical emission spectroscopy and image analysis
Process Metallurgy Research Unit, P.O. Box 4300, FIN-90014
University of Oulu, Finland
Report Series in Physical Sciences No. 136 (2020)

Abstract

Electric arc furnaces (EAFs) and ladle furnaces (LFs) are the main recycling units for scrap metal. With lower CO_2 emissions than traditional ore-based steelmaking, the importance of EAFs can be expected to increase in the future. Increasing steel production rates and demand for high-quality and special steels require innovative process control systems to be developed for the steel industry. However, the harsh conditions inside the furnaces set strict requirements for durability and viable data acquisition methods for online measurement systems.

In this thesis, the applicability of optical emission spectroscopy (OES) as an online measurement system for industrial EAFs and LFs is discussed, based on the results from pilot-scale and industrial EAFs, and an industrial LF.

The electric arc has been characterised with OES, plasma diagnostics, and image analysis in the pilot-scale EAF measurements. These studies highlighted the influence of slag composition on the overall properties of the electric arc, the electrical parameters of the furnace, and the arc length–voltage relation. The majority of the atomic emission lines in the electric arc OES spectra were observed to originate from the slag components.

In the industrial EAF campaign, high alloyed steel grade was observed to have high-quality arc spectra within 30 mins before tapping and higher radiative heat transfer compared with the carbon steel grade. The spectra from the carbon steel grade, on the other hand, were used to observe how spectra evolve during slag foaming. Additionally, the molten bath surface temperature was estimated from the OES spectra. The slag composition was evaluated with OES in the industrial LF campaign, indicating that the CaF_2, MgO, and MnO content of the slag could be evaluated from the spectra.

Key words: OES, plasma diagnostics, electric arc furnace, ladle furnace,
online analysis, slag composition, process monitoring

Pauna, Henri Tapani: Valokaaren karakterisointi ja uuniprosessien seuranta optisella emissiospektroskopialla ja kuva-analyysillä
Prosessimetallurgian tutkimusyksikkö, postilokero 4300, 90014
Oulun yliopisto, Suomi
Fysiikan julkaisusarjat No. 136 (2020)

Tiivistelmä

Valokaari- ja senkkauunit ovat metalliromun tärkeimmät kierrätysyksiköt. Valokaariuunien merkityksen odotetaan kasvavan tulevaisuudessa alhaisempien hiilidioksidipäästöjen takia verrattuna perinteiseen malmipohjaiseen teräksenvalmistukseen. Teräksen tuotantomäärien kasvu sekä korkealaatuisten ja erikoisterästen kysyntä vaativat innovatiivisten prosessinohjausjärjestelmien kehittämistä terästeollisuudelle. Uunien kovat olosuhteet asettavat kuitenkin tiukat vaatimukset reaaliaikaisten mittausjärjestelmien kestävyydelle ja toteuttamiskelpoisille mittausmenetelmille.

Tässä opinnäytetyössä tutkittiin optisen emissiospektroskopian (OES) soveltuvuutta on-line-mittausjärjestelmäksi teollisille valokaari- ja senkkauuneille pilottimittakaavan valokaariuunin sekä teollisen valokaari- ja senkkauunin tulosten perusteella.

Valokaari on karakterisoitu OES:llä, plasmadiagnostiikalla ja kuva-analyysillä pilottimittakaavan valokaariuunimittauksissa. Nämä tutkimukset korostivat kuonan koostumuksen vaikutusta valokaaren ominaisuuksiin, uunin sähköisiin parametreihin sekä kaaren pituuden ja jännitteen suhteeseen. Suurimman osan kaaren OES-spektrien emissiopiikeistä havaittiin olevan peräisin kuonakomponenteista.

Teollisessa valokaariuunikampanjassa korkeaseosteisella teräslaadulla havaittiin korkealaatuisia valokaarispektrejä 30 minuutin kuluessa ennen kaatoa sekä korkeampi säteilylämmönsiirto verrattuna hiiliteräslaatuun. Hiiliteräslaatujen spektrejä käytettiin puolestaan spektrien kehittymisen tarkkailuun kuonan vaahdotuksen aikana. Lisäksi sulapinnan lämpötila arvioi-tiin OES-spektrien perusteella. Kuonan koostumus arvioitiin OES:llä teollisessa senkkauunikampanjassa, mikä osoitti, että kuonan CaF_2-, MgO- ja MnO-pitoisuudet voitiin arvioida spektreistä.

Asiasanat: OES, plasmadiagnostiikka, valokaariuuni, senkkauuni, reaaliaikainen analyysi, kuonan koostumus, prosessiseuranta

Acknowledgments

This dissertation was completed between 2017 and 2020 in the Process Metallurgy Research Unit at the University of Oulu. The funding for the first two years of my research was granted by the European Union “On-line slag composition analysis for electric arc furnaces” (OSCANEAF) project under the Research Fund for Carbon and Steel. The project ended in June 2019, after which I was involved in the Symbiosis of metals production and nature (SYMMET) and Platform economy in refining metal (AMET) projects. The completion of my last two articles and doctoral thesis was funded by two post-graduate grants from the Association of Finnish Steel and Metal Producers operating under the Technology Industries of Finland Centennial Foundation. During the years, I had the opportunity to attend conferences in Venice and Düsseldorf, the second of which was financially supported by the University of Oulu Graduate School 2019 travel grant.

The international collaboration in the OSCANEAF project meant I had the opportunity to work with personnel from RWTH Aachen University (Germany), the Royal Institute of Technology (Sweden), Luxmet Oy (Finland), Outokumpu Stainless (Finland), and Deutsche Edelstahlwerke GmbH (Germany). It has been a privilege to learn from these experts in electric steelmaking, both in academia and in the steel factories. Luxmet Oy provided the measurement equipment and analysis software, the laboratory and pilot-scale experiments helped me to understand what was going on with the arcs, and the industrial campaigns with the application prospects gave the research an ambitious purpose. Special thanks belong to Thomas Willms and Thomas Echterhof from Aachen, Mikko Jokinen from Luxmet Oy, Niko Hyttinen from Outokumpu Stainless, and Jonas Seehausen and Jens-Sebastian Klung from Deutsche Edelstahlwerke GmbH. Without your help, I wouldn’t have a dissertation to defend.

At the University of Oulu, my work was conducted as a collaboration between the Process Metallurgy Research Unit and the Nano and Molecular Systems Research Unit. This arrangement served as a foundation for very interesting discussions and future development ideas for my research. I wish to thank my supervisors, Prof. Timo Fabritius, Prof. Marko Huttula, and Dr Matti Aula for all the teaching and support they gave me during these years. Timo and Matti, I thank you both for the lessons and guidance concerning the fascinating field of process metallurgy. Without you, this dissertation would not exist, and I would never even have heard of the term “process metallurgy”. Marko, thank you for this collaboration that has lasted more than eight years. It has been an honour to complete my Bachelor’s, Master’s, and now, finally, doctoral degrees with your help.

I wish to thank my colleagues in the Process Metallurgy Research Unit for accepting a physicist within their ranks. I hope it has been as joyful for you all as it has been for me. I owe huge thanks to Dr Eetu-Pekka Heikkinen, who taught me more in two months than I learned in two years on my own. I thank my follow-up group members Prof. Matti Alatalo, who is also an excellent guitarist, and Dr Ville-Valtteri Visuri for ensuring I was on the right track from both the physics and metallurgy perspectives. I greatly appreciate the work of Associate Professor Anders Tilliander and Professor Jianhua Liu in the pre-examination of my dissertation. Your feedback and expertise gave me more confidence in this thesis.

Lastly, my thanks belong to my friends and family, who I think still don’t quite know what I do. I have tried to explain, but maybe it’s enough that they know it has something to do with plasma and steelmaking. I want to thank my mother Anne, father Pekka, and sister Janika for always being there to help me and giving me a shelter in Rovaniemi to return to. I want to thank Jenna for sharing her life and enthusiasm for music with me. To my family and my friends: your support has been unimaginably important.

Oulu, September 2020 Henri Pauna

LIST OF ORIGINAL PAPERS

This thesis is based on the following peer-reviewed articles:

I. Pauna H, Willms T, Aula M, Echterhof T, Huttula M, Fabritius T (2019) Pilot-scale AC electric arc furnace plasma characterization. Plasma Research Express. 1(3): 035007.

II. Pauna H, Willms T, Aula M, Echterhof T, Huttula M, Fabritius T (2020) Electric arc length-voltage and conductivity characteristics in a pilot-scale AC electric arc furnace. Metallurgical and Materials Transactions B. 51(4): 1646-1655.

III. Pauna H, Aula M, Seehausen J, Klung J-S, Huttula M, Fabritius T (2020) Optical emission spectroscopy as an on-line analysis method in industrial electric arc furnaces. Steel Research International. 2000051. Article published online https://doi.org/10.1002/srin.202000051.

IV. Pauna H, Aula M, Seehausen J, Klung J-S, Huttula M, Fabritius T (2020) Industrial Ladle Furnace Slag Composition Analysis with Optical Emissions from the Arc. ISIJ International. Advance online publication https://doi.org/10.2355/isijinternational.ISIJINT-2019-676.

As the main author of the publications listed above, I had the responsibility for the OES, plasma, and image analyses, the OES slag composition evaluation, and writing the articles. The experiments were conducted in collaboration with the coauthors.

Other related publications by author:

1. Pauna H, Willms T, Aula M, Echterhof T, Fabritius T (2018) Prospects of plasma analysis for electric arc furnaces. Proceedings of the 7th International Congress on Science and Technology of Steelmaking, Associazione Italiana di Metallurgia, Venice, Italy.

2. Aula M, Pauna H, Andersson N Å I, Jonsson C Y C, Fabritius T (2018) Arc plasma emerging from the foaming slag – Plasma diagnostics and visual observations. Proceedings of the 7th International Congress on Science and Technology of Steelmaking, Associazione Italiana di Metallurgia, Venice, Italy.

3. Pauna H, Aula M, Seehausen J, Klung J-S, Huttula M, Fabritius T (2019) Development of process control for industrial electric arc furnaces with optical emission spectroscopy. Proceedings of 4th European Steel Technology and Application Days, Congress Centre Düsseldorf, Düsseldorf, Germany.

Contents

Chapter 1

Introduction

1.1 Electric arc furnace and ladle furnace

Approximately a third of global crude steel is produced with electric arc furnaces (EAFs). The EAF is the main operating unit in electric steelmaking, covering the steelmaking steps from raw material to the tapping of the molten steel. The charge material of the EAF, which is usually a combination of recycled metal and e.g. direct reduced iron (DRI) or hot briquette iron (HBI), is melted by an electric discharge between the furnace electrodes and the metal. At the end of the heating, the molten metal is poured into a ladle, which is transported to a ladle furnace (LF) for refinement.

The amount of steel that is produced via electric steelmaking can be expected to increase in future due to restrictions on carbon dioxide emissions. Odenthal *et al.* state that the CO_2 emissions of EAF and blast furnace routes are 395 and 1,744 kg per tonne of steel respectively, with 30% lower energy consumption with the EAF route [1]. When natural gas is used as a reductant to produce DRI or HBI for the EAF process, the CO_2 emissions vary from 466 to 1,140 kg CO_2 per tonne of steel, depending on the ratios of DRI, HBI, pig iron, and scrap metal [2].

The expected increase in steel production and the demand for high-quality and special steels pose new challenges for the electric steel industry. One of the downsides of using scrap metal as charge material is the varying quality and composition of the recycled metal, which affect both the slag and steel compositions. Thus, the increase in electric steelmaking will prompt a demand for more sophisticated measurement systems in the EAFs and LFs for more reliable and stable steel production. The harsh atmosphere and extreme temperatures in the furnaces set a strict operating window for the measurement equipment and analysis methods, and viable online *in situ* measurement systems are therefore scarce.

1.2 Objectives and scope

Online *in situ* measurement solutions for electric steelmaking are a necessary step for the development of more dynamic process control and the improvement of current practices. With online analysis, the furnace operator can react in real time to abnormal changes in the process, optimise the timing of e.g. carbon and oxygen injections, and monitor the slag composition and molten bath properties. The implementation of an online measurement system would therefore improve both resource and energy use, and help to prevent the accumulation of alloying elements and iron in the slag.

A promising candidate for an online measurement system is optical emission spectroscopy (OES), in which the optical emissions from the electric arc and the heat radiation are measured. Studies have shown that OES can be used to evaluate some major slag components from the electric arc spectra [3–5], and monitor the melting of the scrap and slag surface conditions in an industrial EAF [6]. The measurement equipment withstands the furnace conditions and consists only of spectrometers, a measurement head, optical fibres, and a data storage computer. In a general set-up, the optical fibres, which guide the light to the spectrometers, are attached to the measurement head, which is aligned towards the electric arc. OES is applicable both in EAFs and LFs, since both furnaces use electric arcs in the process.

In this thesis, the electric arcs are analysed and discussed from the perspective of the applicability of OES for an online measurement system for EAFs and LFs. The aim is to present data validation tools for OES, and to study the benefits and limits of OES in industrial applications. In the industrial applications of OES, the focus is on slag composition analysis. The impurities of the steel are accumulated in the slag, and hence the reaction chemistry of the slag must be carefully controlled during the melting process. Thus, online analysis of the slag composition with OES would be a major improvement compared with common x-ray fluorescence (XRF) slag composition analysis, which is performed offline after slag sampling and sample preparation.

The original publications of this thesis present pilot-scale AC EAF measurements (Papers I and II), an industrial EAF campaign (Paper III), and an industrial LF campaign (Paper IV). These papers are summarised in Table 1.1. The pilot-scale measurements were conducted to characterise the arc plasma with respect to the physical dimensions of the arc, and to identify the relation between the length of the arc, the electrical data of the furnace, and the slag composition. All these aspects bring new insights to the industrial applications, because the electric arc cannot be seen or easily directly measured in the industrial furnace. The electrical parameters are practically the only variables that can be used to change the furnace operation. The industrial EAF measurements were conducted to identify when OES could be used to evaluate the slag composition and to further develop the data validation tool with plasma diagnostics. Due to the versatile usability of OES, the molten bath surface temperature and the intensity distribution of the radiation were also determined from the spectra. The industrial EAF campaign consisted of both high alloyed and carbon steel grades, which allowed a study of the differences between the optical emissions of these two grades. The industrial LF campaign showed that the CaF_2, MgO, and MnO content of the slag could be evaluated with the OES measurements and plasma diagnostics. Furthermore, phase transition calculations were performed to evaluate the composition of the plasma at different plasma temperatures.

Table 1.1: The relationship of the publications with the research.

	Paper I	Paper II	Paper III	Paper IV
Furnace	Pilot-scale EAF	Pilot-scale EAF	Industrial EAF	Industrial LF
Method	OES, XRF, image analysis	XRF, image analysis	OES	OES, XRF, phase transition calculation
Topic	Plasma characterisation	Electrical properties of the arc	OES, plasma, temperature	Plasma analysis, slag composition

Chapter 2

Methods and theoretical background

2.1 Optical emission spectroscopy

2.1.1 Atomic structure, electronic transition, and optical emission

Atoms consist of positively charged protons and neutral neutrons in the nucleus, which is surrounded by negatively charged electrons. Quantum mechanical treatment of particles gives raise to an energy state structure in which electrons are distributed to different energy states, or orbitals. The electrons are the fundamental species in the OES phenomena, because the optical emissions are attributed to the electron transitions between energy states. The first four orbitals are named s, p, d, and f, which can be occupied by 2, 6, 10, and 14 electrons respectively [7]. The ground state of an atom is the energy state structure in which the energy of the atom cannot be further lowered by transitions of electrons to lower energy states. For molecules, the situation is more complicated, because the atoms are bound to the molecule and can move relative to each other, giving rise to rotational and vibrational energy states and transitions [8].

The energy state structures and the occupation of the orbitals by the electrons are not arbitrary, but follow Hund's rules and Pauli's exclusion principle [9]. The ground state occupation of orbitals by the electrons follow Hund's rules, which describe the energies related to each occupation of an energy state by an electron. Pauli's exclusion principle, on the other hand, sets the restrictions to the allowed occupation of the energy states by the electrons. The electronic transitions between the energy states follow specific selection rules that indicate which transitions can occur, and which are forbidden [7]. Hence, Hund's rules, Pauli's exclusion principle, and the selection rules depict both the energy state structures of the particles and the electronic transitions allowed for the particle.

An optical emission is a process in which a particle releases excess energy as a photon to eventually reach the ground state. The process starts with the absorption of energy, which excites an electron from a lower energy state to a higher energy state. This excited state is not stable due to its excess energy compared with the ground state, and the excitation will therefore decay to a lower energy state. The energy is released as a photon with energy equivalent to the energy difference between the upper and lower energy states. An example of the energy state structure of atomic neutral calcium is presented in Figure 2.1, with electronic transitions between energy states. The energy of the photon is related to its wavelength, because

$$E = \frac{hc}{\lambda}, \tag{2.1}$$

where E is the energy, h is Planck's constant, c is the speed of light, and λ is the wavelength. The transition from the upper to lower energy state can also occur in another state than the initial state.

A neutral particle consists of an equal number of electrons and protons. If an electron receives enough energy, it can be detached from the particle. The particle is said to be singly positively ionised when it has one fewer electron than protons. If another electron is detached, the particle is doubly positively ionised, and so on. In OES, these ionisation stages are labelled with Roman numerals I, II, III etc. for neutral, singly ionised and doubly ionised species respectively. For example, an

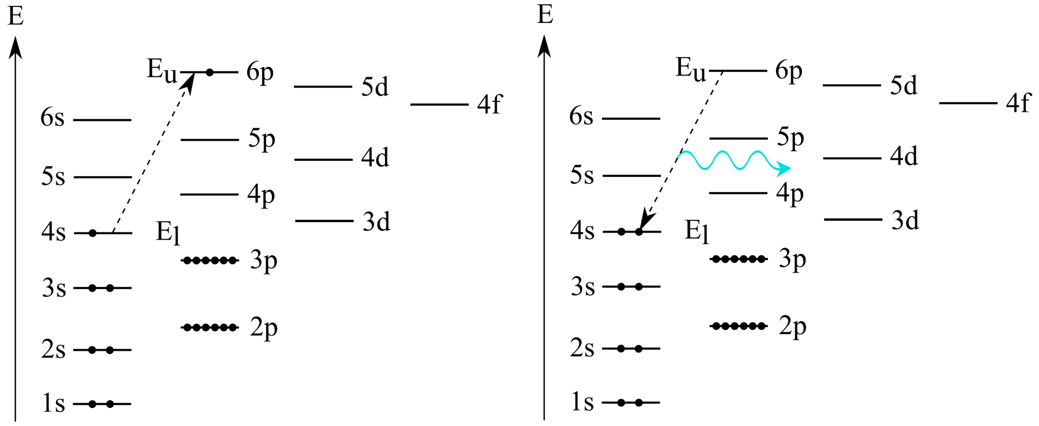

Figure 2.1: The excitation (left) and relaxation (right) energy state diagrams for Ca I emission between the upper and lower energy states 6p and 4s, respectively. E_u stands for upper energy state; E_l for lower energy state. The photon that is emitted in the relaxation has a wavelength of 504.162 nm and is marked by a wavy arrow. Electrons are marked by black dots.

emission line from neutral calcium would be labelled Ca I, and an emission line from singly ionised calcium Ca II. Neutral and ionised species produce different emission spectra even though they are from the same element. This is caused by the changes in the energy state structure of the particle.

When the energy of a system is increased by e.g. increasing the temperature, the higher energy states become more occupied. More and more molecular electronic transitions occur at elevated temperatures in the vibrational and rotational energy states, which produce photons in the infrared region of light. If the temperature is sufficiently high, atomic emissions can also occur in the visible and near-infrared regions. The emissions that arise due to increasing the temperature of the system correspond to heat radiation. The heat radiation is very intensive in EAFs and LFs due to the high temperature of the molten bath and the arc, which means that the heat radiation will create an intense background for the atomic emission spectrum from the arc.

2.1.2 Emission line structure

The emission line that the photons produce for the relaxation in Figure 2.1 is presented in Figure 2.2. The emission line is centered at 504.162 nm with a full width at half maximum (FWHM) of 1.5 nm. The intensity of the emission line is approximated with a fit function, which can be e.g. a Gaussian or Lorentzian function, or their convolution Voigt function [7]. The Gaussian functions used in the research of this thesis follow

$$G(x) = A \times \exp\left(\frac{(x-B)^2}{2C^2}\right), \tag{2.2}$$

where A is the height of the Gaussian, B is the position of the center of the Gaussian, and C is related to the FWHM. The photons from the same electronic transition show dispersion in their energies, which gives raise to the broadening of the emission line. Broadening is affected by many phenomena such as the chemical environment of the emitting species, electromagnetic forces, and the temperature. These effects shift the energy states from the initial energy state structure. When particles from the same element radiate in different environments, most of the radiation occurs at the wavelength corresponding to the undisturbed electronic transition, for which transitions from different radiative environments produce the broadening of the line. For example, the FWHM of the emission line in Figure 2.2 is around 1.5 nm, and the broadening of the line is affected by the high temperature and electric fields on the furnace.

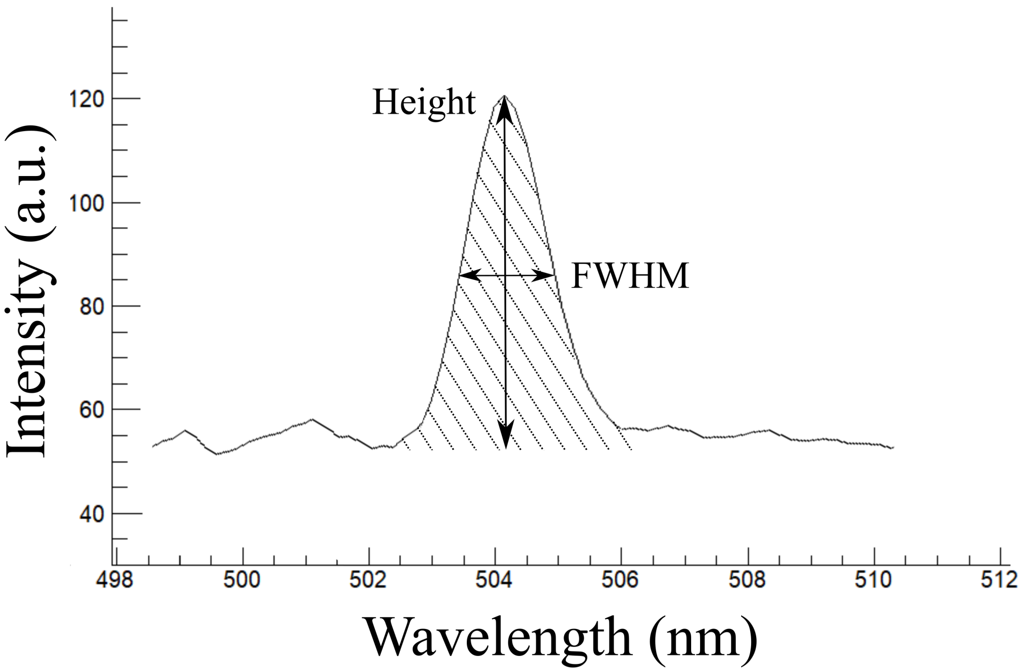

Figure 2.2: Emission line from the 6p → 4s relaxation of calcium. The approximate integrated area of the emission line has been marked with inclined lines.

2.1.3 Identification of light-emitting components from OES spectra

Energy state structures are unique for each element due to the differences in the number of electrons, protons, and neutrons. Thus, the emission lines of an element can be identified based on the observed wavelengths, which are related to the energy of the photon in Equation (2.1). The NIST Atomic Spectra Database, which covers a wide range of atomic emission lines and their line-specific properties, has been used in the work of this thesis to identify the atomic emission lines in the arc spectra [10].

Light that is visible to human eye covers approximately 380 – 740 nm. Ultraviolet light has lower wavelength than 380 nm, whereas near-infrared light has higher wavelength than 740 nm. The three spectrometers used in this thesis are referred to as ultraviolet (UV), visible (VIS), and near-infrared (NIR), covering 247.337 – 419.199 nm, 298.267 – 866.400 nm, and 496.655 – 1048.934 nm respectively. The optical resolution of the spectrometers were 0.047 nm for the UV, 0.156 nm for the VIS, and 0.151 nm for the NIR. Example spectra from all three spectrometers are presented for the pilot-scale EAF, industrial EAF, and industrial LF in Figure 2.3. In the EAF and LF spectra, the spectrum consists of all the emissions from the molten bath and the arc. This means that each arc spectrum has hundreds of emission lines from

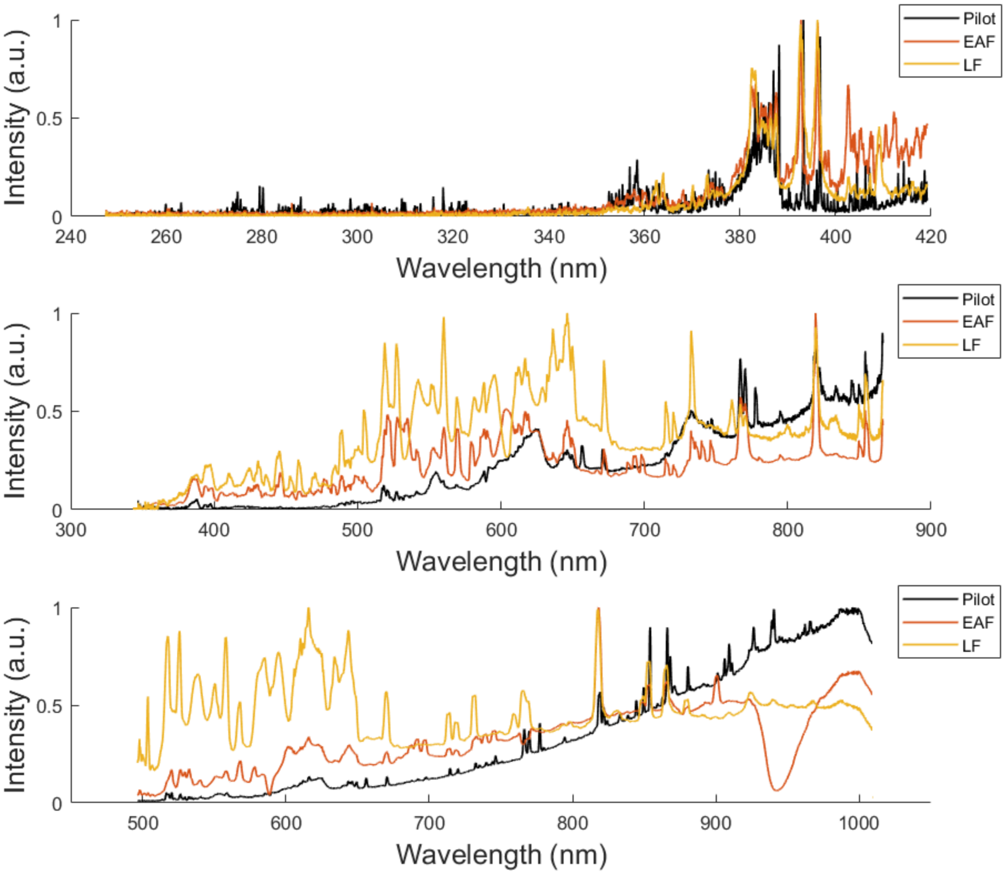

Figure 2.3: Electric arc emission spectra from UV (upper), VIS (middle), and NIR (lower) spectrometers for pilot-scale, industrial EAF, and industrial LF. The intensities have been normalised for comparison purposes.

each atomic and molecular component present in the furnace. The most prominent elements observed in the research of this thesis were from Ca I, Ca II, Mg I, Mn I, Cr I, and Fe I. Al I and Si I could be seen in the pilot-scale spectra below 400 nm, but were not analysable in the industrial spectra. A more sensitive spectrometer would be required to detect the Al I and Si I in the UV range.

It is clear from Figure 2.3 that the atmosphere of the furnace affects the optical emissions. In the pilot-scale spectra, there are several emission lines below 340 nm, whereas the industrial EAF and LF spectra do not have any lines at this low wavelength. UV light is effectively absorbed by the gases, which are produced especially during the melting of the charge material in the industrial furnaces. The visible and near-infrared ranges, on the other hand, receive a lot of light in all three furnaces. Compared with the pilot-scale and industrial EAF spectra, the LF spectrometer receives more light in the visible wavelength range than in the near-infrared. The visibility of the arc was observed to be better in the industrial LF than in the EAF, which explains why the LF spectra have more intensive emission lines from the arc.

2.1.4 Optical thickness and self-absorption

The optical thickness of the arc plasma and the atmosphere affects the observed light intensity at the measurement head. If the medium through which the light travels significantly affects the propagation of the light, i.e. by absorbing or reflecting the light, the medium is said to be optically thick. In the EAF and LF OES measurements, the optical thickness plays a significant role, because it determines in which process steps the optical emission from the arc can be measured.

The high optical thickness of the arc can be observed e.g. as self-absorption, which is a naturally occurring phenomenon that decreases the intensity around the central wavelength of an emission line [7, 11, 12]. In self-absorption, an emitted photon is absorbed by another particle, which is typically of the same element. Self-absorption occurs especially in plasmas with a high concentration of particles within the plasma at different temperatures. The plasma temperature is higher in the core of the plasma than at the edges, and more particles are therefore excited in the core due to higher energy. If a particle in the core of the plasma emits a photon, it can be absorbed by a non-excited particle at the edge of the plasma before the photon escapes the plasma. Theoretically, the photon can now be emitted in an arbitrary direction, which can also be the opposite direction of the original propagation. Furthermore, the excited electron of this newly excited particle can decay to a different lower energy state or release energy via collisional de-excitation, which means that the photon can be emitted at lower energy or not at all [12]. Thus, some of the emitted light can be at least momentarily trapped within the plasma, which in turn decreases the intensity of the emission line at the spectrometer. The self-absorption can be clearly seen in alkali lines, e.g. in the two K I emission lines around 760 nm in the NIR spectrum of the EAF in Figure 2.3. The self-absorption of alkali lines can be so intense that the emission line forms a significant decrease in intensity, which is called self-reversal [7, 12]. It should be noted that certain emission lines, especially intensive resonance lines, may be more prone to self-absorption than weaker emission lines or lines from a different element.

If the atmosphere is optically thick, e.g. due to high gas and dust formation during the melting of the charge material, light may be absorbed by these particles in the atmosphere. The observed intensities at the measurement head therefore decrease. The gas formation rate is very high in the early stages of the EAF process, when the charge material has not yet melted completely. Another source of gases in the EAF and LF atmosphere can be oxygen and carbon injections, which produce e.g. CO gas. The gas particles, either atomic or molecular, emit and absorb light at characteristic wavelengths, as described in Section 2.1.1.

The absorbing effect of the dusts in the atmosphere, on the other hand, depends on the particle size, because the larger particles absorb and scatter light less effectively than the smaller particles [13]. The composition of the dusts depends on the raw materials and processes, and can include iron oxides, zinc oxides, and slag particles [14–16]. In the computational study of Opitz *et al.* [17], it was discovered that a larger amount of dust in the atmosphere resulted in the absorption of more than half the heat radiation by the gas phase, whereas for the lower amount of dust, approximately 60% of the heat radiation reached the surfaces. It can be therefore be expected that the absorption of light by the dust particles in the atmosphere significantly affects the OES spectra.

2.1.5 Thermal radiation

At elevated temperatures, the thermal energy of the particles increases. This results in e.g. low-energy vibrational and rotational transitions of electrons in molecules, which emit light in the infrared wavelength range. At a given temperature, the intensity as a function of wavelength and temperature follows Planck's law,

$$I(\lambda, T) = \frac{2hc^2}{\lambda^5} \frac{1}{\exp(hc/\lambda kT) - 1}, \tag{2.3}$$

where h is the Planck constant, c is the speed of light, λ is the wavelength, k is the Boltzmann constant, and T is the temperature. An example thermal radiation spectrum from an industrial EAF is presented in Figure 2.4. The drops in intensity around 588 and 760 nm are related to the self-absorption of the resonate Na I and K I lines respectively. The other drops in intensity arise from the absorption of molecular

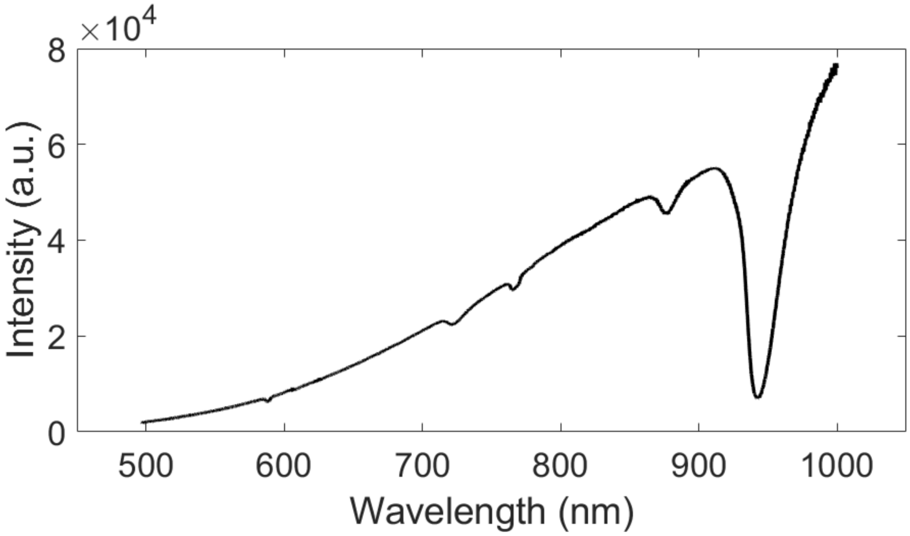

Figure 2.4: Thermal radiation spectrum from an industrial EAF.

species or from spectrometer configurations. However, these aspects are beyond the scope of this thesis.

Since the molten bath temperature of the EAF and LF is more than 1,500 K, the OES spectra will contain a notable background from the thermal radiation. The thermal radiation is a combination of the molten metal bath radiation affected by the radiation and absorption of the atmosphere. Furthermore, if the electric arc is in the view cone of the spectrometer, the thermal radiation increases even more due to the high temperature of the arc. When the arc is not in the view cone of the spectrometer, the thermal background can be used to estimate the molten bath surface temperature. By approximating that the observed temperatures are lower than 5,000 K, Planck's law (2.3) can be used to derive a relation between two wavelengths, their thermal intensities, and the temperature. The temperature under this approximation is

$$T = \left(\frac{1}{\lambda_2} - \frac{1}{\lambda_1}\right) \frac{hc/k}{\ln\left[(I_1/I_2)(\lambda_1/\lambda_2)^5\right]}, \tag{2.4}$$

where subscripts 1 and 2 refer to the selected upper and lower wavelengths respectively. However, since the furnace atmosphere affects the optical thickness and emits its own heat radiation, the temperatures in Equation (2.4) should be treated as estimates, not absolute values. Furthermore, the upper and lower wavelengths should be carefully selected so that alkali or slag component emission lines do not disturb the temperature analysis. As can be seen in Figure 2.4, the thermal spectrum has several self-absorption regions which affect the observed intensity. The λ_1 and λ_2 have been chosen to be 800 and 600 nm respectively, because neither alkali or slag component emission lines reside near these wavelengths.

2.2 Plasma diagnostics

Plasma is a state of matter that consists of free particles, such as electrons, atoms, and molecules. In EAFs and LFs, plasma forms as the high-energy current passes between the electrodes and the molten bath. OES is a suitable method for characterising the plasma, because the electronic structure of the particles, and thus also the wavelengths of the emission lines, are affected by the plasma temperature and electron density.

2.2.1 Plasma temperature

The electric arc plasma temperature is typically around 4,000–5,000 K at the edges, and around 30,000 K in the core of the plasma [18]. At these temperatures, the material evaporated from the molten bath decomposes to its atomic and molecular components, which radiate at their characteristic wavelengths. The plasma temperature can be evaluated from the OES spectra with the Boltzmann plot method [19], which is

$$\ln\left(\frac{\epsilon^z \lambda_{mn}}{g_m A_{mn}}\right) = -\frac{1}{kT} E_m^z + \ln\left(\frac{hcN^z}{4\pi U^z(T)}\right), \tag{2.5}$$

where z is the ionisation state, ϵ is the wavelength-integrated emissivity, λ is the emission line wavelength, subscripts n and m are the lower and upper energy states respectively, g is the degeneracy of the energy state, k is the Boltzmann constant, T is the temperature, E is the energy of the upper energy state, h is the Planck's constant, c is the speed of light, N is the number density, and $U^z(T)$ is the partition function. Once the left-hand side is plotted with respect to the E_m^z for several emission lines from the same element at the same ionisation degree, the plasma temperature can be determined from the slope of the plot. The term on the right-hand side of Equation (2.5) with the natural logarithm can be neglected, because it only adds a constant term to the plot at a fixed temperature.

The error of the Boltzmann equation can be evaluated with

$$\frac{\delta T}{T} = \frac{kT}{\left[\sum_{i=1}^{q} E_i^2 - \frac{1}{q}\left(\sum_{i=1}^{q} E_i\right)^2\right]^{1/2}} \left(\frac{\delta\epsilon}{\epsilon} + \frac{\delta A}{A}\right), \tag{2.6}$$

where q is the number of emission lines, $\delta\epsilon/\epsilon$ is the general relative error of line intensity, and $\delta A/A$ is the general relative error of transition probability [20]. The $\delta\epsilon/\epsilon$ and $\delta A/A$ were approximated as 10% and 20% respectively. The plasma temperature error is very sensitive to the upper-state energies of the emission lines used in the Boltzmann plot. If these energies are close to one another, a high error is expected, because the plot covers only a small energy range. Hence, several lines with varying upper-state energies should be used in the plasma temperature analysis for better accuracy.

2.2.2 Electron density of the plasma

The electron density describes the number of electrons, i.e. the charge carriers, in the plasma. As part of the atoms and molecules is ionised, the electron density of the plasma increases. Electron density can be determined with the Saha-Boltzmann equation [19], which is

$$N_e = C\sqrt{T^3}\frac{I^z_{mn}\lambda^z_{mn}A^{z+1}_{ij}g^{z+1}_i}{I^{z+1}_{ij}\lambda^{z+1}_{ij}A^z_{mn}g^z_m}\exp\frac{E^z_m - E_{\text{ion}} - E^{z+1}_i}{kT}, \tag{2.7}$$

where C is $2(2\pi m_e k)^{3/2}/h^3$, m_e is the mass of electron, I^z is the intensity of emission line, and E_{ion} is the ionisation energy of the ground state. Equation (2.7) combines two emission lines from subsequent ionisation stages, such as neutral and singly ionised. The Saha-Boltzmann equation requires prior knowledge of the plasma temperature, which can be solved using Equation (2.5).

2.2.3 Local thermodynamic equilibrium

Real plasmas are never in total thermodynamic equilibrium, i.e. have uniform energy throughout the plasma, due to disturbances from the environment and the internal forces of the plasma. However, plasmas can be in local thermodynamic equilibrium (LTE), where parts of the plasma can have a very uniform energy distribution. The fulfilment of LTE is attributed to the electron density of the plasma, since the energy of the arc is mainly transferred to electrons, which then distribute the energy within the plasma [21]. The McWhirter criterion for the LTE [19, 22], stating that the collisional processes must be at least ten times the radiative processes, is

$$N_e \geq 1.6 \times 10^{12}\sqrt{T}(\Delta E)^3 \ [\text{cm}^{-3}] \tag{2.8}$$

where ΔE is the energy difference between energy states in electron volts, and T is the temperature in Kelvins. The right-hand side of Equation (2.8) is referred to as $\mathrm{N_{LTE}}$.

2.3 Electric arc image analysis

Images of the electric arc were recorded with a camera in the pilot-scale EAF measurements. The camera was filtered with three standard green light band-pass filters that are used in welding. The frame rate of the camera was 20 images per second. An example arc image is presented in Figure 2.5. In the figure, the electrode glows in the upper-left corner. The hit spot of the arc on the slag surface was determined to be the brightest point of the arc on the slag. The arc length was approximated as the distance between these two coordinates in the image. The length of the arc in Figure 2.5 is 0.21 m. The glow of the slag originates from the heat radiation of the slag and evaporated material in the furnace atmosphere.

The electric arc length is one of the main parameters that can be changed during industrial processes. The arc length is usually changed by changing the voltage, and information on the relation between the length of the arc and the electrical

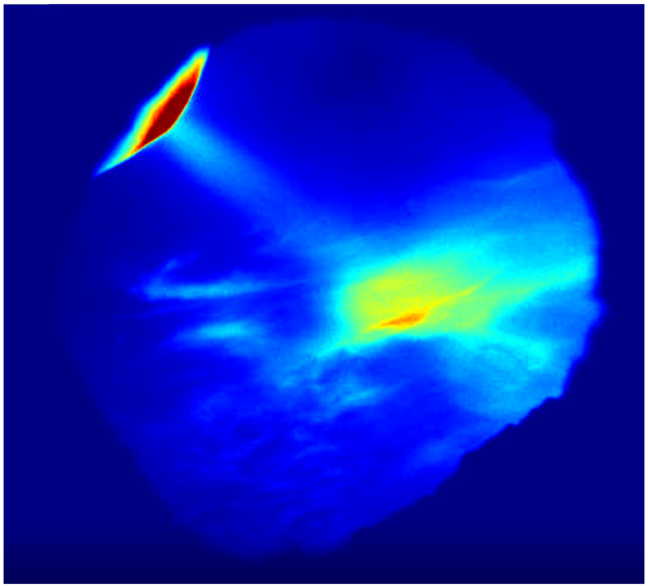

Figure 2.5: Electric arc image from the pilot-scale AC EAF.

parameters of the furnace is thus important. The electrical data of the pilot-scale furnace was recorded once per second to ensure that the physical dimensions of the arc could be attributed to the electrical parameters.

Another interesting topic concerning the electrical parameters is how the composition of the slag affects the arc–bath interactions. The image analysis can be used to link the physical dimensions of the arc to the electrical data of the furnace, which in turn can be related to the slag composition. The slag composition for several measurement periods was determined with XRF to study the relation between the slag composition and the voltage. By studying the electrical data with respect to the length of the arc, theoretical relations presented in other studies can also be reviewed and evaluated.

Chapter 3

Electric steelmaking

3.1 Electric furnace operating parameters

In electric steelmaking, the majority of the steel is produced in AC EAFs [23]. Compared with DC furnaces, the advantages of AC furnaces are lower investment costs, and AC furnaces do not have a bottom electrode that requires regular changing [1]. The furnaces used in the research of this thesis were AC furnaces. The discussion presented in the following therefore focuses on the AC furnaces.

3.2 AC EAF and process steps with corresponding spectra

An industrial AC EAF is schematically presented in Figure 3.1. The upper shell is omitted for display purposes. The refractory mass and bricks protect the vessel from the molten bath, whereas the water-cooled panels direct the heat energy away from the walls and roof of the furnace. As the charge material melts, gases are evaporated throughout the melting process. These gases are directed out of the furnace via the off-gas extraction system, from which the energy in the gas can be recovered. When all the charge material is molten, the steel is tapped out of the EAF with a tapping spout into a ladle for secondary metallurgy.

The example spectra in this section were recorded during the industrial EAF campaign that was conducted in the research of this thesis. Before the EAF melting process, the raw material is charged to the EAF vessel, and the furnace roof is lowered. The two first process steps are the arc ignition and boring of electrodes to the charge, which are presented in Figure 3.2 and 3.3 respectively, with corresponding NIR spectra. The electrodes are lowered to the charge, and the electric arcs are ignited. After arc ignition, practically only reflections of light are received by the spectrometer, because the solid charge blocks the view. When the electrodes have been drilled into the charge, visible light and heat radiation is also received by the

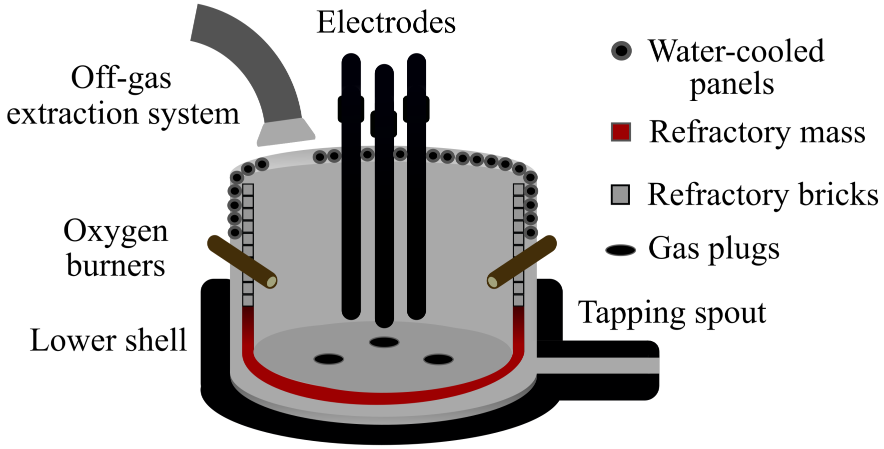

Figure 3.1: Schematic presentation of an industrial EAF.

spectrometer.

After boring, the melt starts to form, and the spectrometer receives more light, as depicted in Figure 3.4. Na I and K I emission lines around 588 nm and 760 nm respectively are clearly seen in the spectra. These emission lines, with Li I and usually also Rb I, are always present in the EAF and LF spectra. Although the alkali components e.g. in the slag are very scarce, they are optically very active, producing very intensive emission lines despite their low concentration.

The spectrometer receives light, depending on the momentary view cone on the melt surface and in the arcs. During the main heating period in Figure 3.5, the spec-

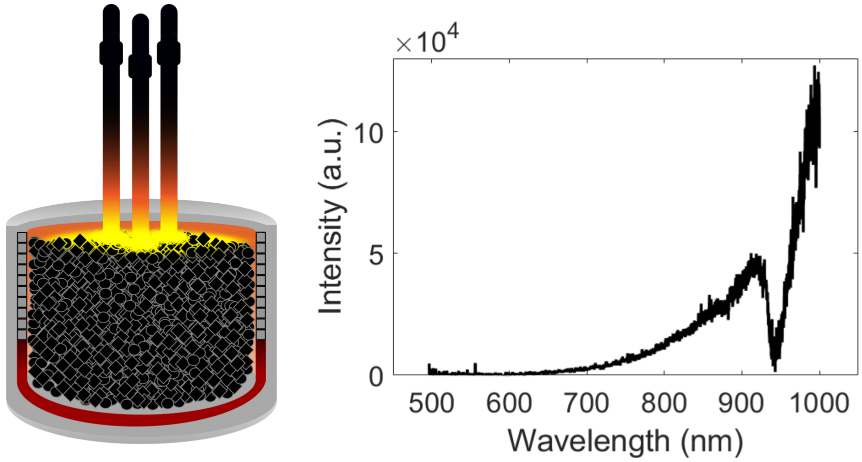

Figure 3.2: EAF ignition and corresponding NIR spectrum. Only reflections of light are received by the measurement head due to solid scrap that blocks the view-cone.

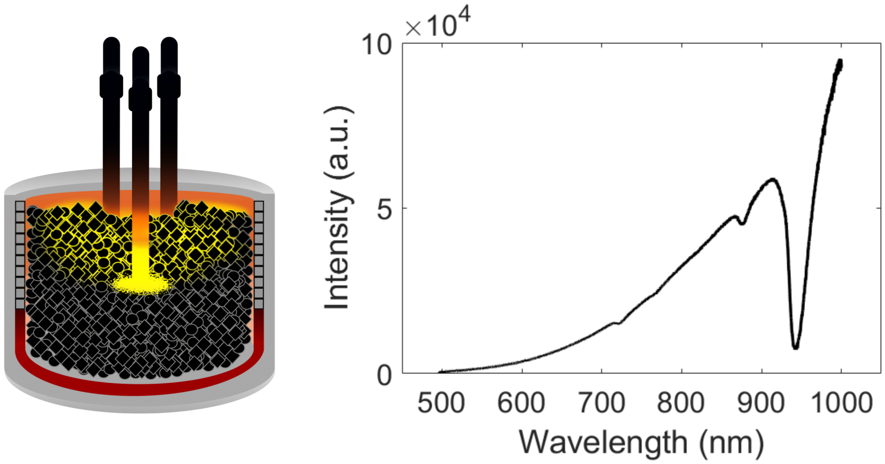

Figure 3.3: Boring and corresponding NIR spectrum. Some visible light and heat radiation reaches the measurement head.

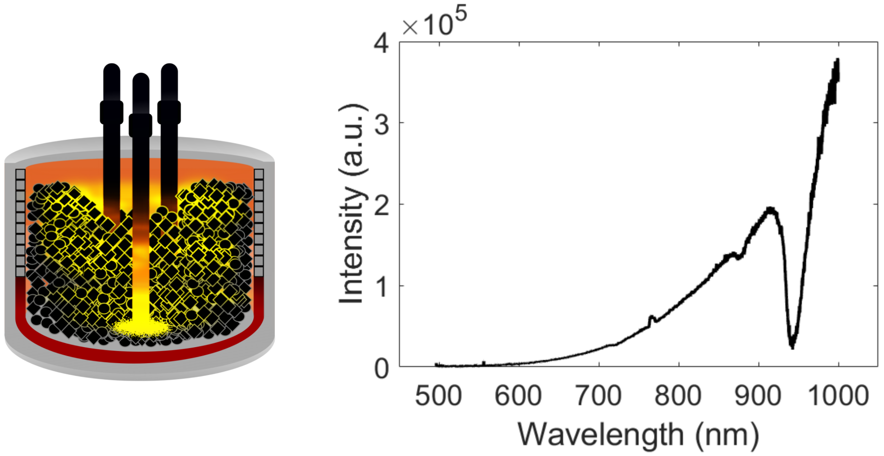

Figure 3.4: Formation of the melt and corresponding NIR spectrum. The measurement head starts to receive more light as the charge material melts. Alkali emission lines, such as K I lines around 760 nm, are seen at this point.

trometer receives less light than in Figure 3.5, probably because the scrap from the sides has collapsed, blocking the view into the melt. In Figure 3.5, the alkali emission lines are clearly affected by self-absorption, as can be seen from the decreases in spectrum intensities at the alkali emission line wavelengths. In the down-melting period in Figure 3.6, the light intensity increases, and the arc can be seen momentarily. However, the spectrum is usually highly affected by the gases that absorb light and distort the spectrum. The self-absorption of alkali lines is even more prominent,

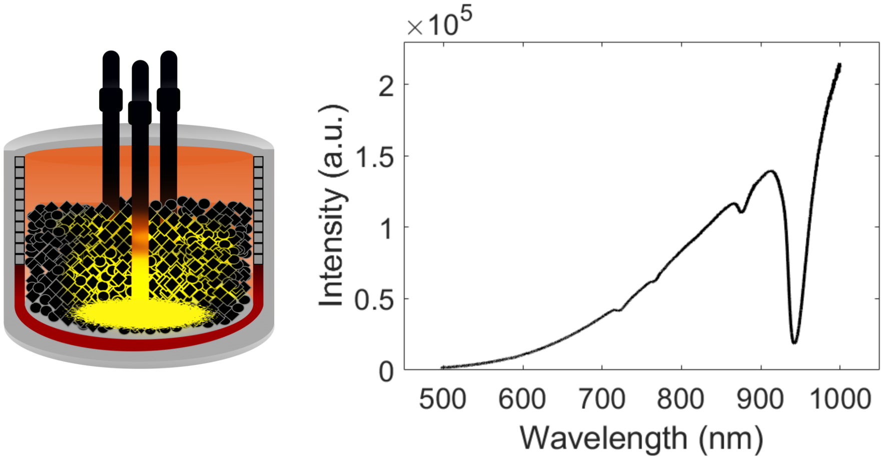

Figure 3.5: Main heating period and corresponding NIR spectrum. Alkali emission lines are observed to be affected by the self-absorption, which can be seen as drops in intensities in the alkali emission wavelengths.

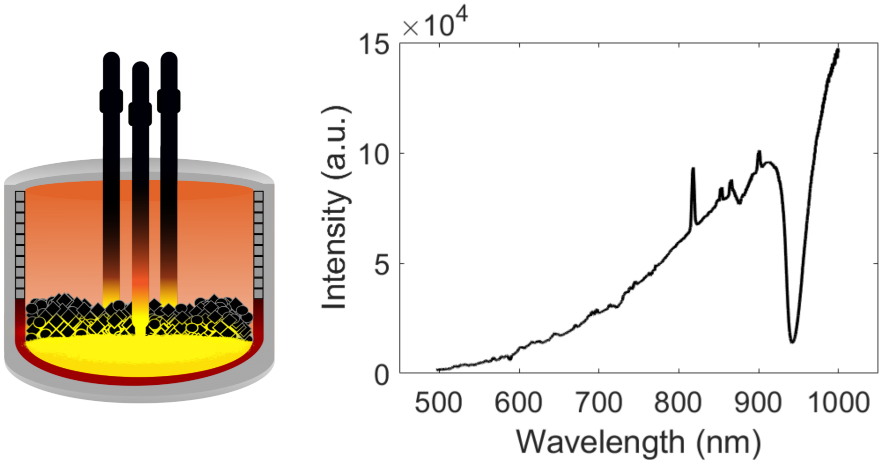

Figure 3.6: Down-melting period and corresponding NIR spectrum. Most of the scrap is molten and measurement head receives faint emissions from the electric arc. The alkali emission lines are usually significantly affected by the self-absorption.

because the spectrum intensity shows a significant decrease in the wavelengths of the alkali emission lines. This is one reason emission lines close to the alkali lines should not be used for OES analyses.

The view cone for the arc is clear in the flat bath period in Figure 3.7. The emission lines from the slag components can now be seen in the spectra. The flat

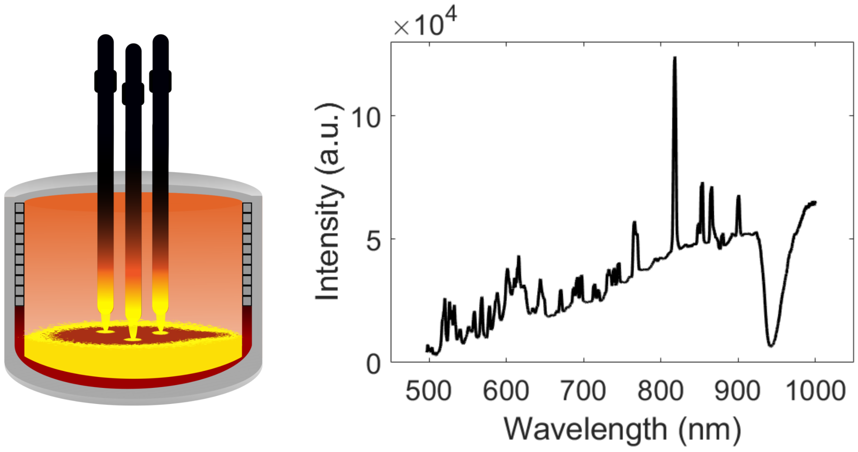

Figure 3.7: Heating and flat bath period with corresponding NIR spectrum. The electric arc emission spectrum is clearly seen with an abundance of emission lines from the atomic slag components.

bath period is the most optimal for OES diagnostics, because the arc is clearly seen and the formation of gases has settled. At this point, the bath has had time to mix, and the slag composition is closer to the final slag composition at tapping. However, when foamy slag practice is used to cover the arcs in order to reduce the radiative heat losses and protect the furnace lining, the arcs may be covered with foam, and the arc spectra cannot be observed.

3.3 Secondary metallurgy with the LF

Usually, the steel composition achieved in the EAF does not meet the quality standards, the chemical composition of the desired final product, and the required melt temperature. The molten metal from the EAF can be further refined in the LF. The operating principle of an AC LF is close to that of an AC EAF, because both these industrial furnaces usually have three electrodes. The purpose of LF treatment is to remove impurities such as H, N, O, P, and S from the steel, modify or remove inclusions, and adjust the melt temperature for continuous casting [24]. In the LF, the melt can be homogenised by stirring, which can be done e.g. by blowing inert argon gas through bottom plugs into the melt. In this process, the steel temperature is also homogenised. The homogenisation of the slag and steel ensures conditions that are suitable for deoxidation, dephosphorisation, desulphurisation, and other practices.

Additive materials such as SiO_2, Al_2O_3, MgO, CaO, and CaF_2 are usually added to the melt to affect the chemical environment of the slag and steel [25]. For example, flux, which consists of CaO and CaF_2, can be added for better desulphurization of the steel. Another important purpose of additive materials is to adjust the basicity and viscosity of the slag to produce optimal conditions for impurity extraction from the steel [26, 27]. Calcium treatment is usually done to alter the morphology of inclusions.

The OES conditions in the LF are very similar to the EAF flat bath period, as depicted in Figure 3.7. However, the LF lacks any solid charge material in the furnace, and the slag is not foamed. The additions of alloying elements and additive materials produce gases as the material melts, and the optical properties, i.e. the optical thickness, thus changes during and after the additions. The gases may absorb the incident radiation, and the arc spectrum can therefore be distorted, and the emission lines very broad. The OES measurements are most efficient before and after the additions have been made, and the atmosphere and gas formation have settled.

3.4 Slag in electric steelmaking

3.4.1 Role and significance of slag in steelmaking

Slag is always present in all steelmaking routes due to impurities in the recycled metal, DRI, HBI, ores, and other raw materials. The slag accumulates on top of the steel due to the density difference between the steel and slag components. The slag plays a key role both in the EAF process and LF refinement, because slag properties affect how the impurities are transferred from the steel to the slag. There are several ways in which the furnace operator can affect slag composition, but the lack of online slag composition analysis brings its challenges to the adjustment of both the amount and the optimal injection instances of additive materials.

The impurities are accumulated in the slag from the steel. The initial slag composition is essentially determined by the composition of the charge material, and the slag composition is changed so that the slag is molten at steelmaking temperatures. Slag composition can be changed by adding basic or acidic slag components, e.g. during the ladle treatment. The main properties of the slag are its basicity and viscosity, which play a significant role in the formation of the slag. It is important to adjust the basicity of the slag to optimal value, because the furnace lining may dissolve into the slag if there is a driving force for its dissolution. This driving force can be decreased by adding MgO to the slag, and the driving force is negligible if the slag is already saturated with magnesium [28]. Low slag viscosity, on the other hand, may result in slag splashes and increased wear of the lining material.

3.4.2 Slag foaming

In carbon steel grades, where a foaming slag practice is usually used, the role of slag is even more important. In foaming slag practice, e.g. carbon is injected into the melt to produce CO bubbles, forming a foamy structure on top of the molten bath once the bubbles reach the slag surface. The arcs are covered at least partially by the foaming slag, reducing heat losses via radiation. This practice also protects the furnace walls and roof from the thermal radiation.

Foaming can be induced by injecting gases such as argon, oxygen, or carbon into the furnace. When adding oxygen and carbon, the chemical reactions essentially include FeO reacting with C, producing Fe and CO. CO can also be related to C reacting with O_2, and CO can further react with CO_2 via reactions with C [29]. Since the FeO plays a significant role in the foaming slag practice, the FeO content of the foamy slag can be relatively high, exceeding 20% [1, 29].

The basicity and viscosity of the slag affect the foaming conditions, because too high a basicity and too low a viscosity do not produce stable foaming conditions [30]. The amount of oxygen and carbon injections must be adjusted to optimal levels, because oxygen injection that is too high or too low results in FeO that is too high or too low in the slag respectively, decreasing foamability [31]. In slags with a similar composition to EAF and LF slags, it has been observed that increasing the FeO content of the slag decreases viscosity, which explains the foam instability with higher FeO content [32]. The work of Lotun and Pilon [33] compares experimental foam thickness with theoretical ones up to 0.5 m. The foam height varies for different slags and practices with which the foam is generated. Since the purpose of the foam is to cover the arcs and reduce heat losses, it can be assumed that the arcs are well covered during foaming.

3.4.3 Slag components

Table 3.1 compiles some basic oxygen furnace (BOF), EAF and LF slag composition ranges from various sources. Generally, the most abundant slag components are those of calcium and silicon. CaO and CaF_2 are also common additive materials in the EAF and LF processes [34–37]. Aluminium is used e.g. as an alloying element and to remove oxygen from the steel, and Al_2O_3 is a typical slag component. Magnesium can occupy a major fraction of the slag composition, especially if it has dissolved from the refractory material. Manganese, which is an alloying element in the steel, is usually present in the slag at lower concentrations of several percentages. The iron and chromium content of the slag can vary significantly in different process steps, and it is affected by the raw material and steel type produced. Fluorine is usually present in the LF slag due to additions of CaF_2, and CaS due to reactions between S and CaO. In some slags, zinc and titanium are also present. Other slag components worth mentioning are those that contain carbon and alkaline metals.

Table 3.1: General slag composition ranges in wt% for BOF, EAF carbon steel grade (EAF C), EAF high alloyed steel grade (EAF H), and the LF.

Component	BOF	EAF C	EAF H	LF
CaO	30-55^{a}	35-60^{b}	39-45^{b}	40-50^{c}*
SiO_2	8-20^{a}	9-20^{b}	9-20^{b}	5-15^{c}*
Al_2O_3	1-6^{a}	2-9^{b}	2-9^{b}	25-30^{c}*
MgO	5-15^{a}	5-15^{b}	5-15^{b}	5-15^{c}*
FeO	10-35^{a}	15-30^{b}	1-6^{b}	0.5-1.5^{c}*
MnO	2-8^{a}	3-8^{b}	0.4-2^{b}	¡1.5^{c}*
S**	0.05-0.15^{a}	0.05-0.15^{b}	0.1-0.3^{b}	0.5-2^{c}*
P**	0.2-2^{a}	0.2-2^{b}	0.01-0.07^{b}	¡0.02^{c}*
Cr**	0.1-0.5^{a}	-	¡5^{d}	¡5
CaF_2	-	-	-	0-30***

a = Fisher *et al.* [38], b = Liang *et al.* [39], c = Tabatabaei *et al.* [40], d = Lin *et al.* [41], e = Huaiwei *et al.* [42], * = at the beginning of LF treatment, ** = either atomic or compound, *** = highly dependent on the CaF_2 additions

The components and their relative ratios present in the slag depend on the practices utilised during the melting. If these practices are optimal, the accumulation of iron, chromium, and alloying elements in the slag can be mitigated. However, if the practices are not carefully planned, valuable alloying elements may dissolve into the slag. Furthermore, poor slag composition may even damage the furnace itself, because a basicity that is too low causes the refractory lining to dissolve into the melt [29].

3.4.4 Slag composition analysis for EAFs and LFs

XRF is a common offline slag composition analysis method in industrial steel plants. XRF requires slag sampling, which is first cooled and then grinded. The prepared sample is then irradiated with X-rays. The X-rays excite the core electrons of the atoms and molecules in the sample. These excited states decay to lower energy states, producing element-sensitive spectra. The slag components are then identified from these spectra. The difference with OES is that the electrons that are excited in OES usually reside in the outermost orbitals, whereas the high energy X-rays excite the electrons in the XRF in the innermost orbitals.

XRF analysis is time consuming due to sampling and sample preparation. The results of the XRF cannot be used directly to modify the batch from which the sample is taken, but instead to check the slag composition and adjust the process for the next melt. It is, however, a widely accepted and reliable slag composition analysis method. Hence, even if the slag composition is made using another method, it would still be worthwhile to perform the XRF analysis as well, and use it as reference and calibration data.

The electric arc plasma radiates continuously throughout the furnace operation. Since the OES arc spectra have an abundance of intensive emission lines from the slag components, OES shows prospects for online applicability in slag composition analysis. Plasma analysis, on the other hand, is a promising candidate as an OES data validation tool, since plasma diagnostics can be determined from the spectra. The OES data must first be calibrated with reference data, for which e.g. the standard XRF analysis is ideal. XRF is widely used in the steel industry, so it is reasonable to relate OES to something that is already used and understood by the operators.

3.4.5 Internal use, recycling, and commercialization of slags

In the electric steelmaking route, both EAF and LF slags are a major by-product. Internal reuse of slags has gained interest in the industry because it will decrease waste generation and provide alternatives for fluxes [25]. The internal reuse of slags, however, may prove difficult due to the varying composition of the slags, which in turn results in unknown process behaviour and changing product properties [43]. Internal reuse at a steel plant can use the slag in the processes as a slag former. For example, slag with a high CaO and MgO content may be suitable for such purposes [43]. From the perspective of energy savings, Lee and Sohn [44] have proposed that harnessing the waste energy of the slags would be necessary for the continuous viability of the EAF technology due to e.g. increasing electricity costs.

The valorisation of the slags in all the steelmaking routes plays a key role in better waste management and the circular economy [45]. Slags from the steel industry are already used for cement and concrete [45–47], fertilisers [47], and road construction [48–50]. It should be noted that it is very important to know the slag composition before recycling, because harmful constituents, such as those of chromium, can dissolve from the slag products into the soil. This emphasises the importance of reliable slag composition analysis from the slag commercialisation perspective.

Chapter 4

Experiments

Three furnaces were used in the research of this thesis. The furnaces were a pilot-scale AC EAF, an industrial AC EAF, and an industrial AC LF. The spectrometers were AvaspecULS2048, provided by Luxmet Oy. The same spectrometers were used in all the measurements. The emission lines were fitted with special spectrum analysis software made by Luxmet Oy. The software was optimised to analyse a large number of subsequent spectra.

4.1 Pilot-scale EAF measurements

4.1.1 Furnace and measurement set-up

A pilot-scale AC EAF at RWTH Aachen University in Germany was used in the measurements. A schematic of the furnace and measurement set-up is presented in Figure 4.1. The view cone into the furnace is depicted with the green circle and lines. The capacity of the furnace was 200 kg liquid steel, and it was equipped with two graphite electrodes with a diameter of 0.1 m. The furnace was capable of mimicking industrial processes such as charging, boring, melting, and the flat bath period. A Baumer single-lens reflex camera and three spectrometers looked into the furnace via the same opening in the side of the furnace through UV-transparent glass. The camera was filtered with three standard green light band pass filters used in welding.

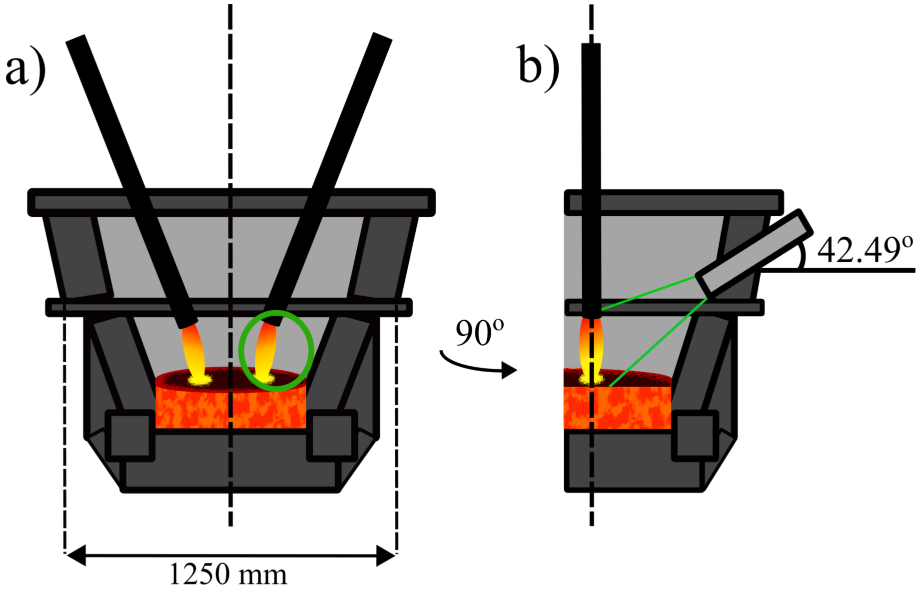

Figure 4.1: Schematic presentation of the pilot-scale AC EAF [Paper I, reprinted under the CC BY 3.0 license].

4.1.2 Description of the measurements

At the beginning of each measurement day, steel scrap and slag formers were charged into the furnace. Once the charge had melted and slag had formed, additive materials such as CaO, Al_2O_3, and SiO_2 were added and left to melt. These materials were added several times a day, and a slag sample was taken before each addition. The compositions of these slag samples were analysed with XRF. The spectrometers and camera recorded 20 spectra and images per second respectively.

4.1.3 Image analysis

The purpose of the image analysis was to determine the physical dimensions of the arc and relate them to the furnace's plasma diagnostics and electrical data. During the data analysis, it was found that the slag composition affected the furnace's electrical parameters, which in turn altered the length-voltage characteristics. Electric arc length is a fundamental process parameter in industrial practices, because changing the arc length is one of the few ways the operator can affect the melting process. It is therefore important to understand the relations between the electric arc with both plasma diagnostics and the electrical data.

A Matlab code was programmed and used to analyse the electric arc images. The steps of the image analysis code are presented in Figure 4.2. The code initially requires the information on the images such as file formats, time stamp information, and frame rate. All the images are converted to greyscale to average the three

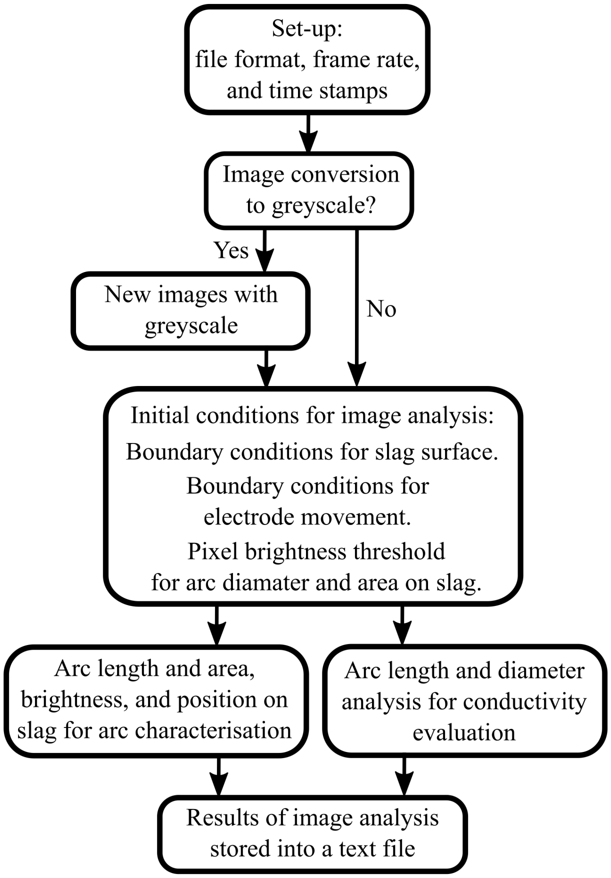

Figure 4.2: Simplified steps of the image analysis code.

RGB brightness values to a single brightness value. The code allows the user to set boundary conditions for the location of the electrode, slag surface, and edges of the view cone into the furnace. The pixel threshold values for the arc length, area, brightness, and diameter are received as user inputs. The code saves the image analysis results as text files or Matlab cells.

The parameters that were studied with the image analysis were arc length, arc diameter, the brightness of the arc on the slag surface, and the area of the arc on the slag, based on a brightness threshold. The arc length was approximated as the distance between the brightest pixels (pxs) on the electrode and the slag. The arc area on the slag was estimated with the pixels that had brightness values of at least 90% of the central brightness value located at the arc length coordinate on the slag. The arc diameter was estimated along the arc axis individually for each arc axis pixel with the pixels that had a brightness value of more than 50 in the standard brightness range of red, green, and blue (RGB) pixels, ranging from 0 to 255.

The position of the arc on the slag was also monitored, because the arc wandered considerably on the slag surface, especially with an arc length longer than 0.15 m. In turn, this significantly influenced the arc length-voltage correlation. Because of this, only the periods with the most stable arcs were viable for the length-voltage analysis. The wandering of the arc on the slag had several causes, e.g. the furnace lining had not dried sufficiently on some of the measurement periods, and the electrical conductivity of the lining was therefore higher than anticipated. The arcs also experienced a repelling force from each other. In the case of three electrodes, the arcs would be more confined to their third of the molten bath surface due to two repelling forces from each arc. In the case of two electrodes, however, the arcs may have wandered on half the molten bath surface.

4.1.4 Developing data analysis tools for OES and plasma analysis

The purpose of the pilot-scale EAF OES measurements was to identify the most relevant phenomena that affected the spectra in an EAF. The pilot-scale OES data was used to develop and optimise self-made Matlab codes for both the emission line and plasma analyses. The codes use text files that contain user-defined emission lines or line ratios, with which the analysis is performed. The codes were developed so that the read-out of the input files and data was sufficiently fast for possible online applications.

The steps of the plasma analysis code are presented in Figure 4.3. The code was automatised to analyse the plasma temperatures, electron density, and LTE criterion density according to the user input. The code was tested with different methods and equations for plasma analysis such as the Stark broadening and shift, Boltzmann equation and plot, Saha-Boltzmann equation, and McWhirter LTE criterion. For industrial practices with harsh conditions, the Boltzmann plot method, Saha-Boltzmann equation, and McWhirter LTE criterion equation show the most applicability due to their simplicity. Stark broadening is a viable data analysis tool for electron density evaluation in various laser-induced plasmas [51–53], but the overlap of emission lines and the changing spectrum quality in the EAF and LF spectra were deduced to bring more uncertainty to the Stark analysis than to the Saha-Boltzmann equation.

Another code was constructed to identify suitable emission lines for the OES analysis and perform slag composition analysis using XRF data as the reference data. If too many of the lines in the arc spectra had been fitted, the computation time would have increased to a limit at which online applicability would suffer. Emission line candidates therefore had to be identified in advance so that only the most relevant data was analysed, preferably within a couple of seconds. In addition to the individual emission line analysis, the code could be used to monitor the time-evolution of the spectrum intensities at different wavelength ranges, providing information on the radiative properties of the molten bath and the arc. The steps of the OES code

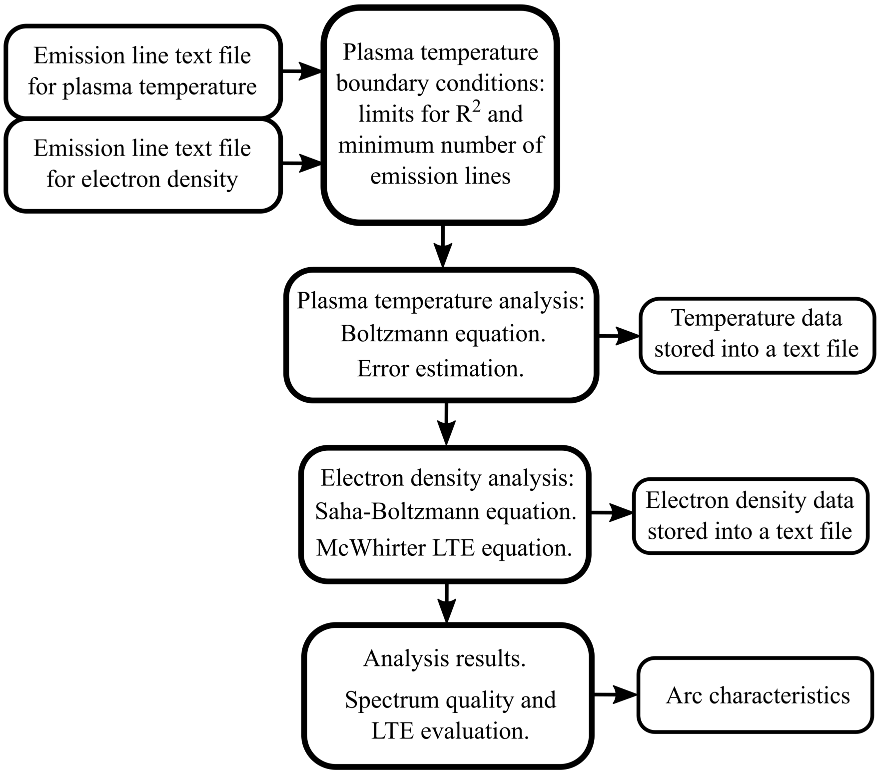

Figure 4.3: Simplified steps of the plasma analysis code.

are presented in Figure 4.4.

The OES codes were observed to fulfil the requirements for fast data analysis from the spectra. If the fitting parameters and the emission lines had been optimised prior to a measurement, the OES data analysis for plasma diagnostics, line ratios, wavelength ranges, and molten bath temperature evaluation could have been completed within a few seconds. The computation time could be decreased if the computation capacity was increased, or parallel computation was used. If more emission lines had been required, e.g. several emission lines for multiple slag elements, the computation time would have increased, especially if the emission lines required deconvolution. In the case of an industrial application, the computation times and data accuracy would have needed to be carefully considered to find a suitable balance between the computation time and analysis accuracy.

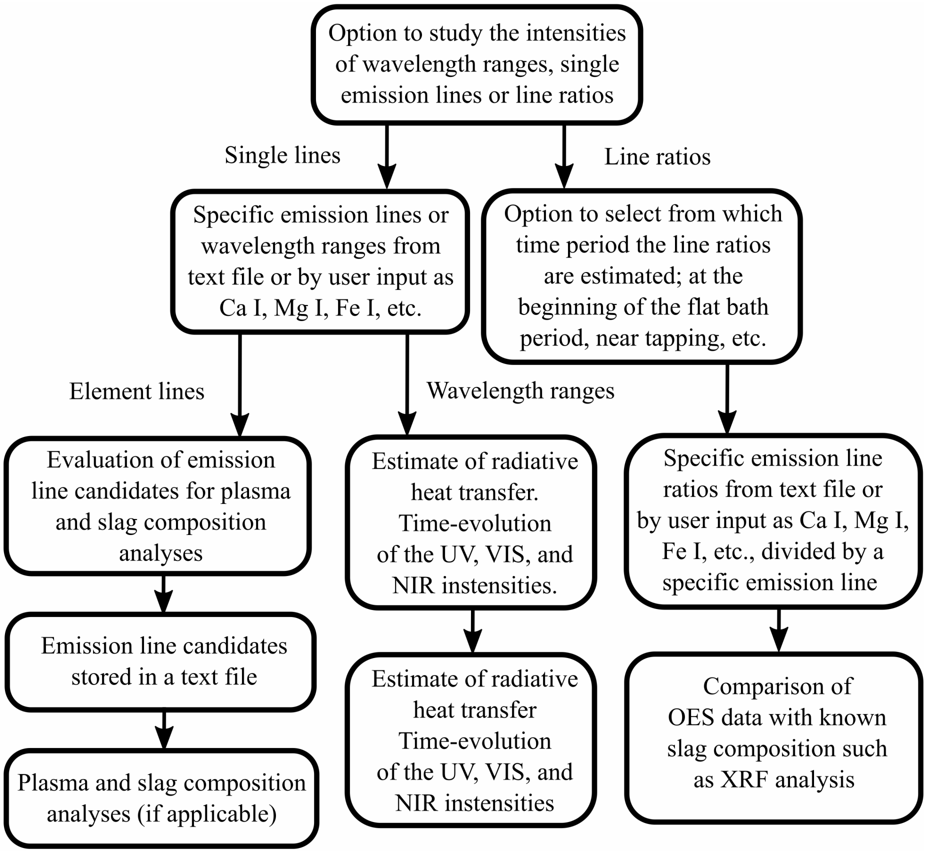

Figure 4.4: Simplified steps of the OES analysis code.

4.2 Industrial EAF and LF campaigns

The industrial EAF and LF campaigns were conducted at Deutsche Edelstahlwerke GmbH, Germany. The capacities of the EAFs were 120 t and 140 t, depending on whether the steel grade was high alloyed or carbon steel grade respectively. The capacity of the LF was 140 t. The furnaces had three electrodes and operated in AC mode.

4.2.1 EAF measurement campaign

Figure 4.5 shows a schematic representation of EAF and OES equipment. The measurement campaign lasted several weeks. Since the furnace lacked any openings through which the spectrometers would see the arcs, a hole was drilled in the furnace panels, after which the edges were welded shut. The measurement head was welded onto the roof to look into the furnace via the drilled hole. Optical fibres were shielded with a protective tube, and the spectrometer cabinet was located near the operator

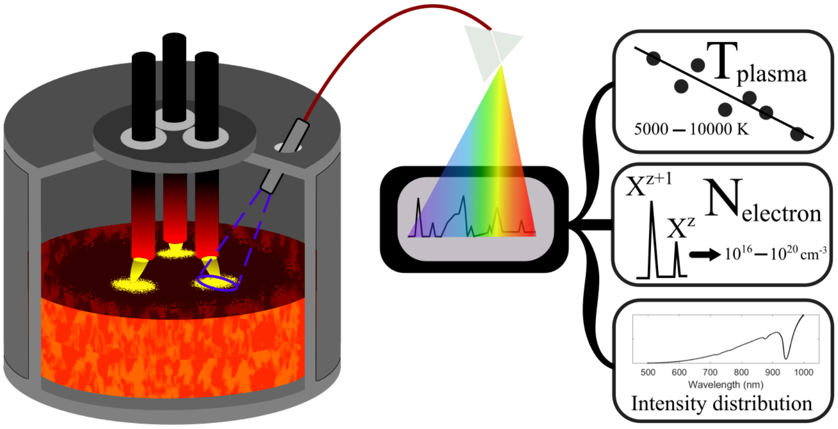

Figure 4.5: Schematic presentation of the industrial EAF and the OES equipment [Paper IV, reprinted by permission of ISIJ International].

room. A pressurised airflow was applied through the protective tube around the optical fibres to cool the measurement head and prevent any slag splashes from reaching it. Both high alloyed and carbon steel grades were produced during the measurement campaign.

The spectra from the NIR spectrometer were used in the OES analysis. The spectra were analysed after the measurement campaign. Both the time-evolution of the intensities of different wavelength ranges and the distribution of the intensities were determined to identify the differences and similarities between the two steel grades. The molten bath temperature was also estimated from the thermal curve of the spectra, using Equation (2.4). Plasma analysis was used as a data validation tool to determine the optimal spectra that could be used for a reliable slag composition analysis. The plasma temperatures were determined for Cr I, Fe I, and Ca I emission lines, using Equation (2.5). The electron density was determined with Ca I and Ca II emission lines, and the Cr I temperature was determined using Equation (2.7). The fulfilment of LTE was studied with Ca I emission lines, and Cr I temperature, using Equation (2.8).

4.2.2 LF measurement campaign

The LF and the OES equipment are schematically presented in Figure 4.6. The measurement campaign lasted several weeks. Three spectrometers, covering UV, VIS, and NIR were used in the campaign. The measurement head was located 5 m from the furnace and looked into it through the gap between the ladle and the roof. The optical fibres were shielded with a protective tube. Although the measurement head was not in contact with the furnace, a pressurised airflow was applied through the protective tube to prevent any slag splashes from reaching the measurement head. Both carbon steel and high alloyed steel grades were produced during the measurement campaign.

The ladles were switched frequently during the measurement campaign as part of standard steel plant procedures. Due to the varying slag compositions and viscosities, the slag accumulated on top of the ladle lining, blocking the view cone into the furnace for some ladles. Hence, not all the heats were analysable. The accumulated slag could be crushed before each heat to ensure a good view into the furnace. This procedure was not used in this LF campaign.

The light acquisition of the VIS and NIR spectrometers was suitable throughout the measurement campaign, but the light intensity was insufficient for the UV spectrometer. A light gathering lens was designed during the campaign and inserted in front of the measurement head to increase the intensity. Consequently, adequate UV arc spectra were observed above 300 nm. However, emission lines below 300 nm were not observable. The low intensity of UV light was attributed to the high absorbance of the UV light by the atmosphere, which significantly decreased the UV emission the spectrometer received. Another reason for low UV intensities was that the measurement head was located several metres from the arcs. The further the light had to propagate, the lower the light intensity was at the measurement

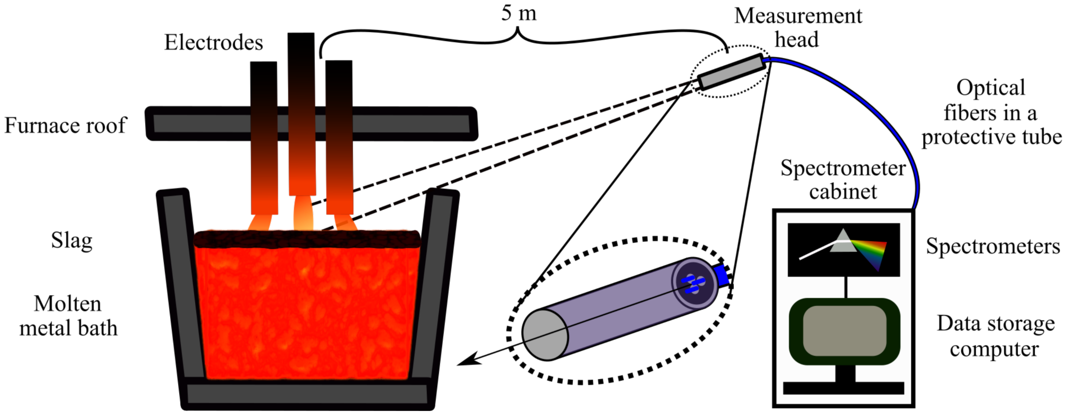

Figure 4.6: Schematic presentation of the industrial LF and the OES equipment [Paper III, reprinted under the CC BY 4.0 license].

head. Furthermore, the probability that the light was absorbed by the atmosphere increased with increasing distance.

The slag composition of the carbon steel grades was determined with XRF as part of the standard steel plant operation. XRF slag compositions of the high alloyed steel grades were unavailable. The spectra from all three spectrometers were analysed after the measurement campaign. The emphasis of the analysis was on the additive material, CaF_2, and lining material, MgO, with MnO. The plasma analysis was used as a validation tool for the spectra and to determine the relation between the Ca I plasma temperature and CaF_2 slag composition.

Chapter 5

Results and discussion

The results of this thesis bring new empirical insight into the electric arc properties during EAF and LF process steps. The pilot-scale tests help to understand the behaviour of the arc and the relations between the slag composition, the electrical parameters of the furnace, and the plasma diagnostics of the arc. The industrial campaigns demonstrate how OES can be used as an industrial application, including slag composition evaluation, monitoring of the radiative heat transfer, and estimation of the molten bath surface temperature. The OES slag composition evaluation and plasma diagnostics are applicable in any electric furnace, provided that the view cone to the arc is sufficient. In radiative heat transfer and molten bath surface temperature estimation, only the molten surface needs to be observable. In addition to the prospects of process monitoring at industrial steel plants, the results also have academic merit that can benefit the modelling of the EAF and LF processes.

5.1 Pilot-scale EAF electric arc plasma characterisation

The electric arc length and the area and brightness on the slag surface were determined from the arc images. An example arc image with the pixel axes is presented in Figure 5.1. The plasma temperatures were observed to be mainly between 4,500 and 9,000 K, and the electron densities between 10^{18} and 10^{20} cm^{-3}. The electron density was observed to exceed the LTE criterion most of the time, but the plasma temperatures derived from different elements may have differed. The differences in plasma temperatures can be attributed to deviation from the LTE [19], which means the plasma temperatures should also be monitored in addition to the electron density.

The slag composition was observed to have a significant effect on some of the slag component emission lines in the plasma analysis. Ca I plasma temperature was affected by the slag's CaO content. If CaO was significantly more than 30%, the Ca I plasma temperature could not be determined with the emission lines that

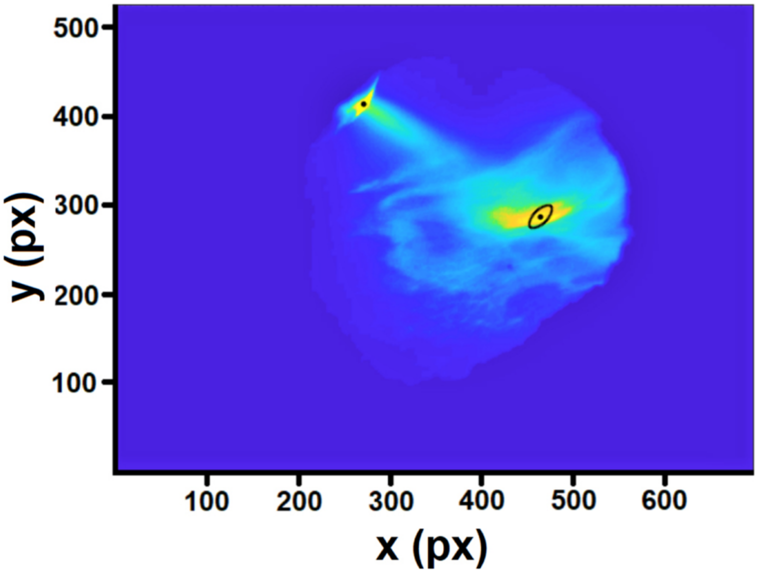

Figure 5.1: An example arc image with an arc length of 16.3 cm. The coordinates for the arc length analysis have been marked with black dots, and the area of the arc on the slag with an ellipse [Paper I, reprinted under the CC BY 3.0 license].

were used. Another aspect that influenced the Ca I plasma temperatures was the high electron densities, which exceeded $2{\times}10^{19}$ cm^{-3}. This was associated with the increasing self-absorption of Ca I lines. The Ca I plasma temperatures were between 4,500 and 6,000 K, and were lower than Cr I and Fe I plasma temperatures, which could mean that the Ca I emissions originated at the edges of the plasma, where the plasma temperature was lower than in the core. The brightness of the arc, however, was saturated with FeO content of more than 35%, meaning high heat transfer via radiation. When FeO was lower than 35%, the brightness of the arc on the slag did not saturate but fluctuated greatly.

A graph for the arc characterisation with the increasing arc length is displayed in Figure 5.2, where FeO is more than 30%, and CaO is close to 20%. The values have been averaged. The standard brightness range of a pixel in an RGB image is from 0 to 255, and brightness B can be observed to be very close to the brightest value, 255. Fe I and Cr I plasma temperatures are considerably more uniform than the Ca I plasma temperature, which fluctuates between 4,000 and 7,500 K. Electron density N_e is several magnitudes more than the LTE criterion density N_{LTE}. Since the plasma temperatures from individual elements do not always agree, deviations from LTE are still observed.

The arc area on the slag surface decreases as the arc length increases, which indicates that the arc diameter also decreases with increasing arc length. The lengthening of the arc also affects the position of the arc on the slag surface, as can be observed

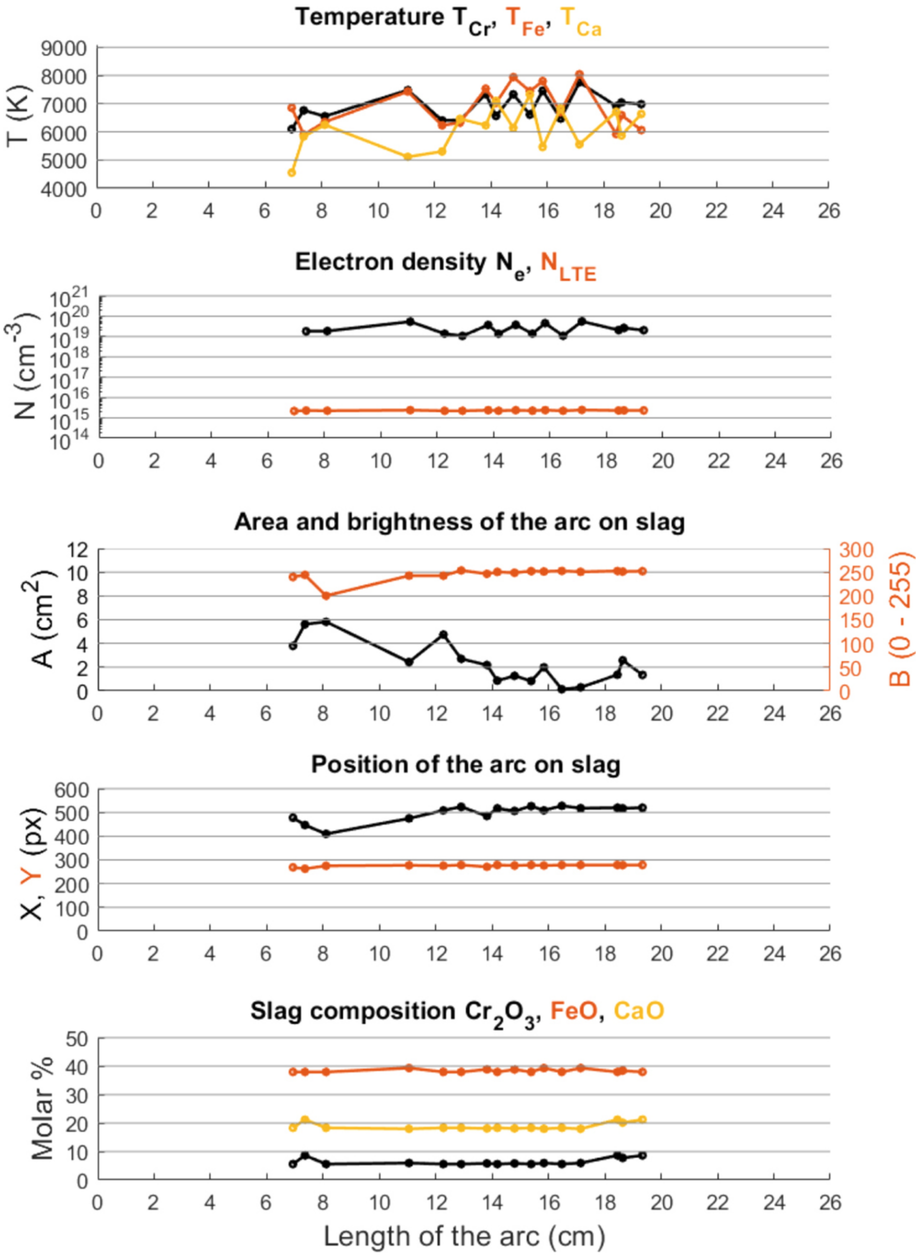

Figure 5.2: Arc properties with increasing arc length when FeO content of the slag is near 40% [Paper I, reprinted under the CC BY 3.0 license].

from the x-component for the position in Figure 5.2. The y-component, which essentially depicts the depth of the images, stays relatively constant with increasing arc length. This means that the arc moves on the slag surface mostly in the x-direction. As can be seen from Figure 4.1 a, movement in the x-direction is either towards or away from the other electrode.

Figure 5.3 displays the arc properties with increasing arc length when FeO was less than 30%, and with CaO ranging from 12 to 33%. The R^2 value of the Boltzmann plot equation (2.5) for Ca I plasma temperatures was less than 0.70, meaning Ca I plasma temperatures could not be determined reliably. The area, brightness, and

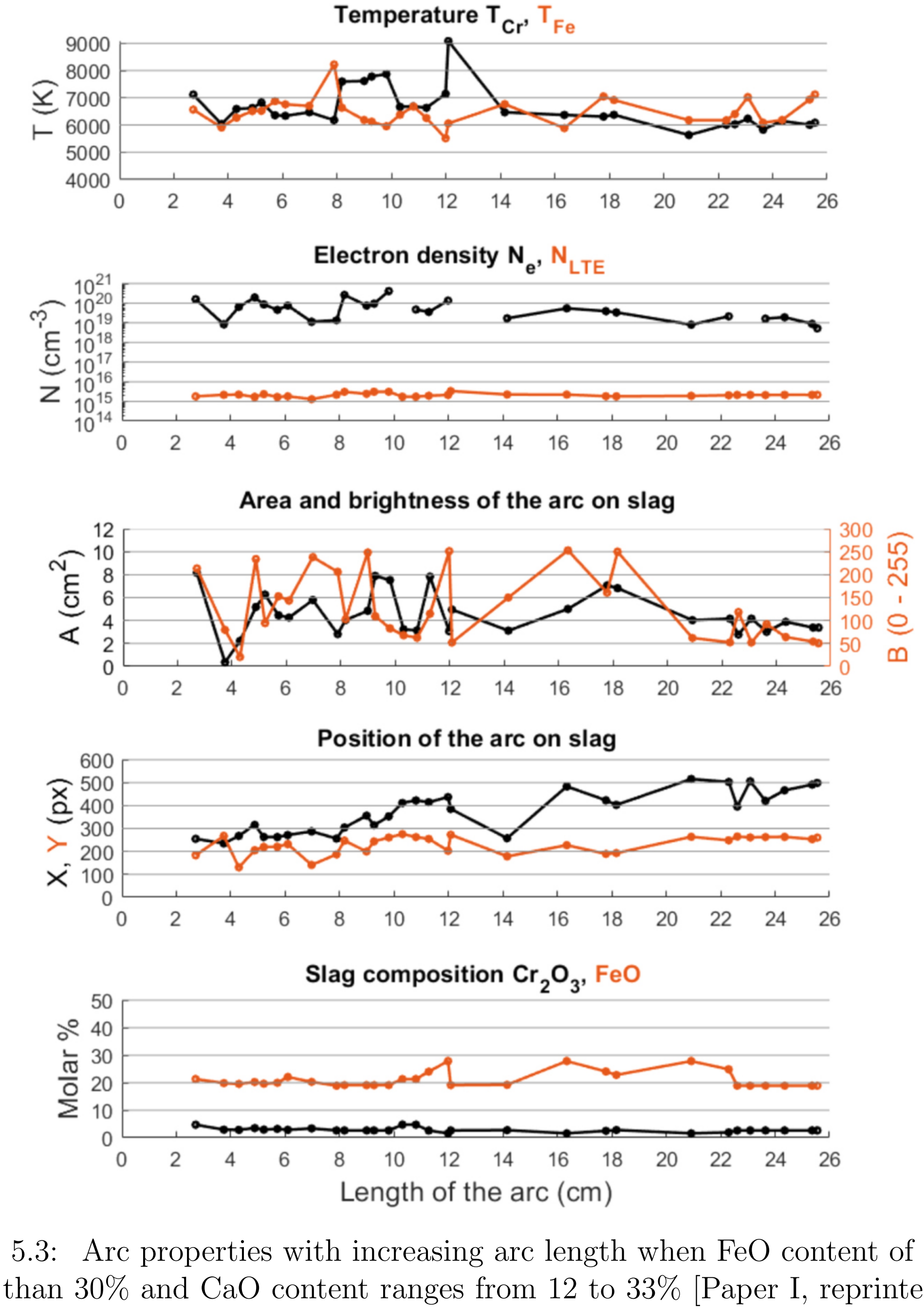

Figure 5.3: Arc properties with increasing arc length when FeO content of the slag is less than 30% and CaO content ranges from 12 to 33% [Paper I, reprinted under the CC BY 3.0 license].

position of the arc on the slag especially deviated from the behaviour in Figure 5.2. The brightness was not saturated, which is attributed to the lower FeO content of the slag. Iron had a significant number of emission lines throughout the spectrum, which also contributed greatly to the overall intensity. A direct link for the arc length with either brightness or the area of the arc on the slag was not found, and these parameters were observed to be more influenced by the slag's momentary properties. Since the slag surface was not rigid, but moved and mixed throughout the melting, the brightness and the area were also observed to change greatly during the measurements.

Regarding plasma analysis, the electron density was not measurable for all arc lengths in Figure 5.3. This can be explained by the Ca I and Ca II emission lines, which were used in the Saha-Boltzmann equation (2.7) for the electron density, because the high CaO content was observed to affect the calcium emission lines, probably via self-absorption. The Cr I and Fe I temperatures were relatively stable for arcs shorter than 8 cm and longer than 14 cm. High fluctuation in the plasma temperatures and a lack of electron density values were observed between these arc lengths. The plasma temperatures were closest to one another between electron densities of 4×10^{19} and 1×10^{20} cm^{-3}. Below or above these values, the temperatures showed fluctuating trends. The general decrease in the electron density with increasing arc length was attributed to the smaller slag volume heated up by the arc for longer arc lengths [54].

The pilot-scale OES research allowed a study of the most prominent phenomena affecting the measured spectra. The main result from this study was that the slag composition could have a major influence on the plasma analysis, and that the observed arc spectra were significantly affected by the furnace atmosphere, the arc's line of sight visibility, and spectrometer configurations. It was noted that it would be very important to optimise the view cone into the furnace so that the set-up would be most suitable for the OES measurements. The spectrometer configurations, namely frame rate and exposure time, must also be considered. For industrial practices, a couple of spectra per second could be more feasible than the 20 spectra per second that was recorded in the pilot-scale measurements. The purpose of the pilot-scale measurements was to link the physical dimensions of the arc to the spectra, which required a higher frame rate due to rapid changes in the arc parameters.

5.2 Electrical properties of the arc in a pilot-scale EAF

It was noted in Paper I's pilot-scale EAF plasma characterisation that the slag composition had a significant effect on spectra and plasma diagnostics. Hence, a study was conducted to identify if the slag composition also affected the electrical properties of the arc. The thermal conductivity of slag is much lower than that of steel, and hence the voltage profile can be affected by varying slag composition. It is important to understand the interaction between the slag and the arc, since the electrical input to the furnace is used to alter e.g. the arc length by changing the voltage. The experiments were performed on three days, referred to as H1, H2, and H3. Fifteen separate measurement periods (Ps) were performed during these days, and plunge tests were performed in eight periods.

The length and diameter of the arc were determined from the arc images, as described in Section 4.1.3. Arc images from a plunge test are displayed in Figure 5.4. Plunge tests, in which the electrode was pushed to the slag surface or plunged into the slag and allowed to rise automatically, were selected for the length-voltage analysis, because these tests showed the most stable arc behaviour. Furthermore, the plunge tests had the widest voltage range, because the electrode position was

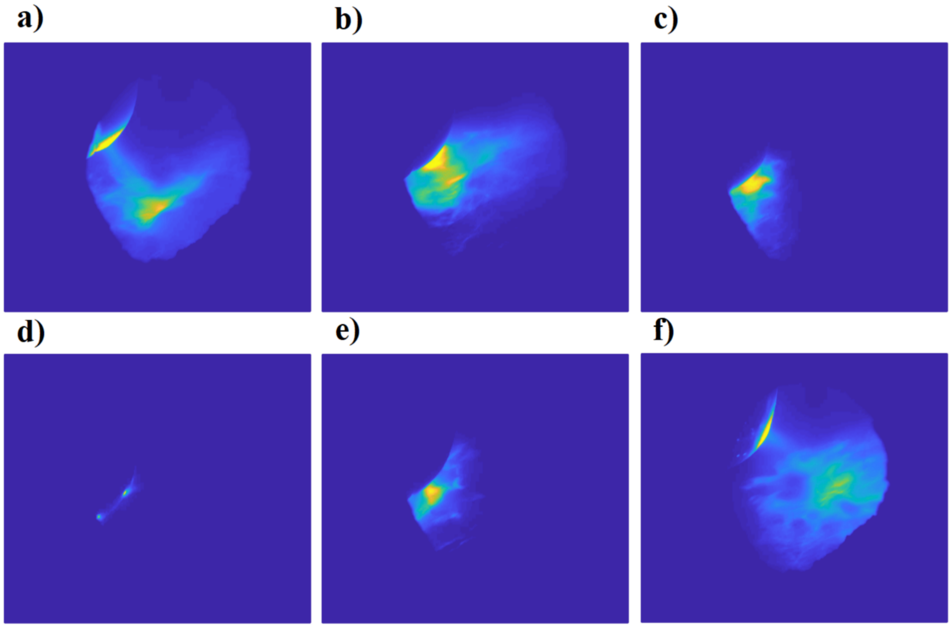

Figure 5.4: Arc images from a plunge test with arc lengths of a) 0.17 m, b) 0.06 m, c) 0.03 m, d) 0.00 m, e) 0.02 m, and f) 0.20 m [Paper II, reprinted under the CC BY 4.0 license].

intentionally changed.

In one plunge test, the electrode was plunged so deeply into the slag that it hit the steel. This instance provided a voltage value of 14.34 V, which was approximated as near the anode-cathode voltage drop, V_{AC}. The resistance of the slag could then be estimated by

$$R_{\mathrm{slag}} = \frac{U_{\mathrm{min}} - 14.34\mathrm{V}}{I} \tag{5.1}$$

where U_{min} was the minimum voltage when the arc was in contact with the slag and I was the current. An intuitive Slag$_{\mathrm{sum}}$ parameter was determined by totalling the components with a positive correlation with the U_{min} and subtracting those with a negative correlation. The Slag$_{\mathrm{sum}}$ is thus FeO + Cr_2O_3 + MnO - (Al_2O_3 + CaO + MgO + SiO_2) in mol%. With these definitions, the values of U_{min} and Slag$_{\mathrm{sum}}$ could be attributed to the changes in the slag composition. These results are displayed in Figure 5.5.

The results of Figure 5.5 show that the slag composition affected the electrical parameters of the furnace. The minimum voltage when the electrode was in contact with the molten bath varied between 50 and 100 V. These were deduced to be relatively high voltages for the V_{AC}, which was expected to be less than 20 V.

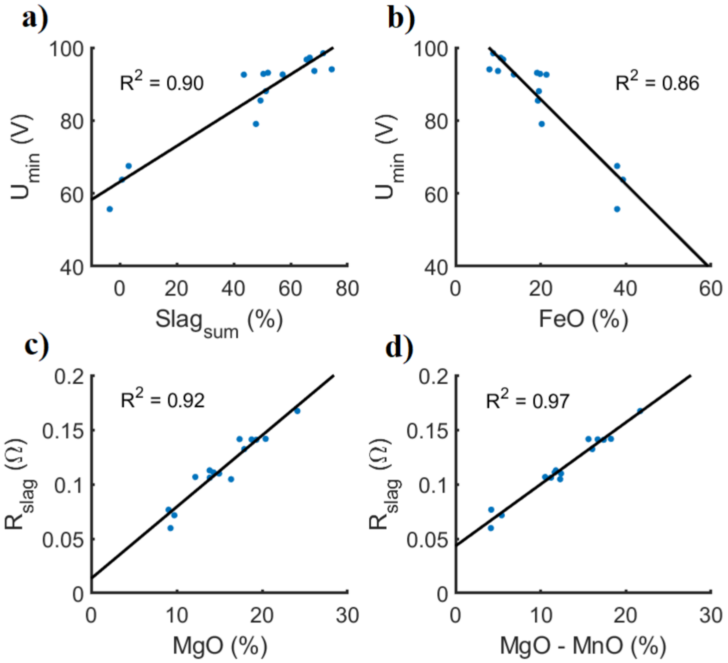

Figure 5.5: Correlations for U_{min} between a) Slag$_{\mathrm{sum}}$ and b) FeO mol%, and R_{slag} between c) MgO mol% and d) MgO mol% - MnO mol% [Paper II, reprinted under the CC BY 4.0 license].

These high voltages were attributed to the interaction of the arc with the slag, and not the steel. By taking into account the slag composition, a relation between the minimum voltage and slag composition could be retrieved. This relation produced a voltage value of 13.98 V, when the slag composition was approximated to consist only of the components that had a positive correlation with respect to the observed minimum voltages. Theoretically, this produced the V_{AC} value of the electrode–steel interaction. The 13.98 V for the V_{AC} was close to the experimental 14.34 V, which was a less than 3% difference from the approximated theoretical value.

The voltage with an increasing arc length is presented in Figure 5.6 for eight plunge tests. The relation between the arc length and voltage was found to be non-linear. The relation between the arc length and the voltage gradient, on the other hand, followed a reciprocal relationship, with R^2 over 0.90 for most cases. These results are displayed in Figure 5.7. The plunge test f) in the Figure 5.6 and 5.7 had the lowest R^2 due to low arc length values observed during the plunge test.

The length-voltage correlation was approximated with

$$U = a \cdot l_{\mathrm{arc}}^{b} + 14.34\mathrm{V} \tag{5.2}$$

and the correlation between length and the voltage gradient V_{g} with

$$V_g = \frac{c - 14.34\mathrm{V}}{l_{\mathrm{arc}}} + d \tag{5.3}$$

where a, b, c, and d were constants. A direct correlation between these constants and

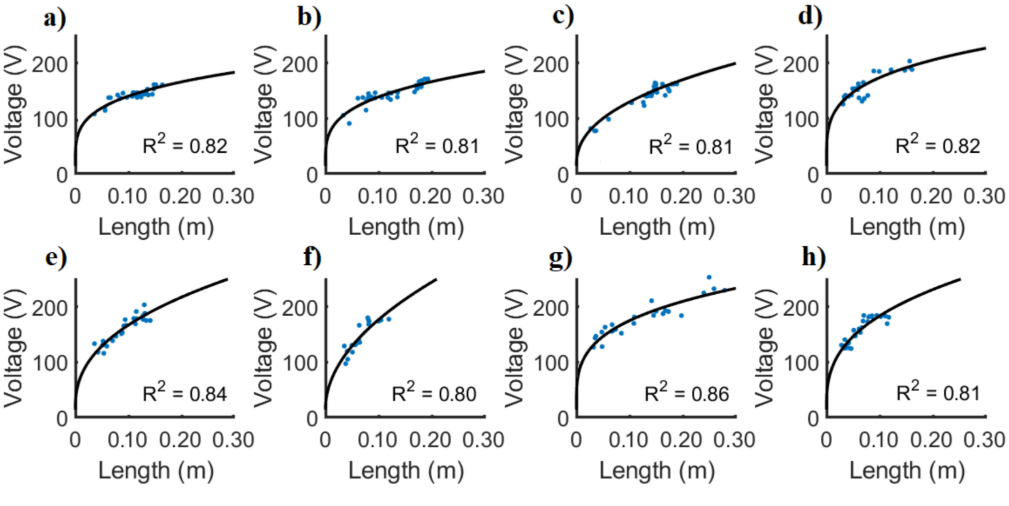

Figure 5.6: Length-voltage correlations for eight separate plunge tests a) H1 P1, b) H1 P2, c) H1 P3, d) H2 P2, e) H2 P3, f) H3 P3 g) H3 P5, and h) H3 P6 [Paper II, reprinted under the CC BY 4.0 license].

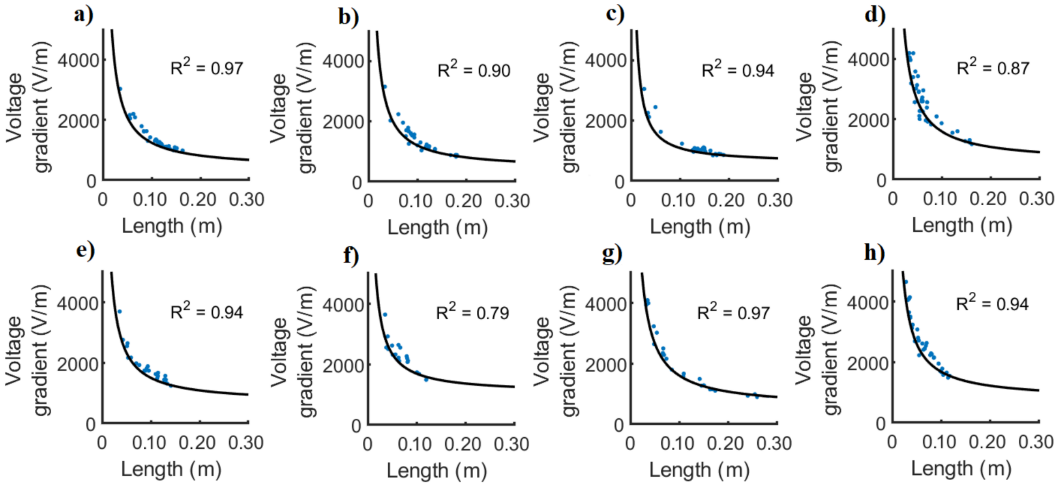

Figure 5.7: Correlations between the arc length and voltage gradient for eight separate plunge tests a) H1 P1, b) H1 P2, c) H1 P3, d) H2 P2, e) H2 P3, f) H3 P3 g) H3 P5, and h) H3 P6 [Paper II, reprinted under the CC BY 4.0 license].

the slag composition could not be determined, but the changes in constants could be attributed to the observed U_{min} values. These results are displayed in Figure 5.8.

The conductivity of the arc was approximated by determining its diameter from the arc images and measuring the resistance across one electrode from the furnace

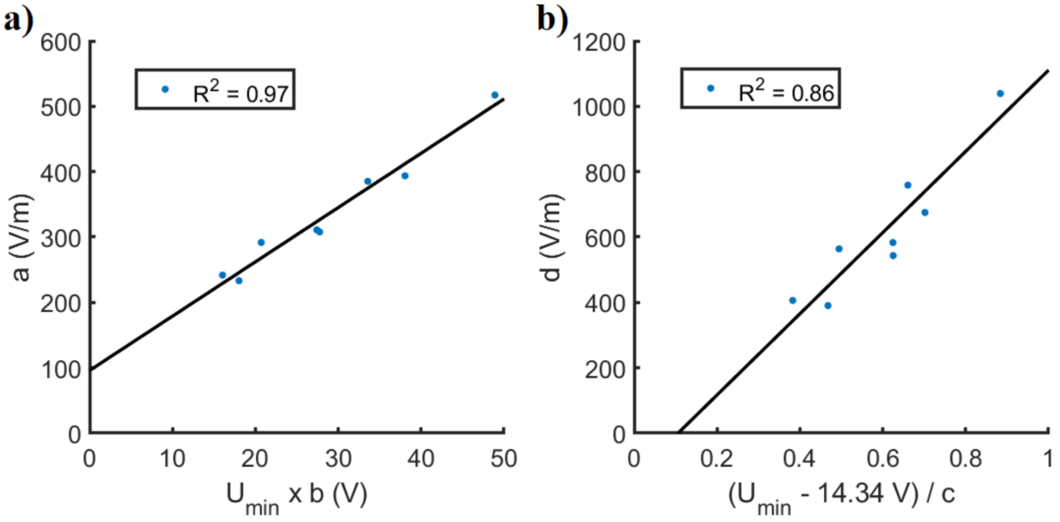

Figure 5.8: Correlations between the constants a) a and b with b) c and d that appear in the Equations (5.2) and (5.3) respectively [Paper II, reprinted under the CC BY 4.0 license].

data. The equation describing this relation is

$$\sigma = \frac{l_{\text{arc}}}{R \times A} \tag{5.4}$$

where R is the resistance, and A the cross-sectional area. The diameter and the cross-sectional area were estimated along the arc axis. However, since the optical and thermal emissions from the slag surface had a distorting effect on the arc diameter evaluation near the slag surface, a 0.02 m section of the arc was used in the analysis. This section of the arc displayed the least interaction with the glow from the slag surface and the atmosphere. The start- and endpoints of this section were 0.03 m and 0.05 m respectively from the electrode coordinate. With this procedure, the conductivity increased as a function of the arc length. The result of the estimated conductivity with an increasing arc length is illustrated in Figure 5.9. The conductivity values are only estimates of the real conductivity, but the results show that the conductivity was generally affected by the arc length and vice versa. Consequently, this relation should be considered when evaluating or computing the conductivity of the arc. However, further experimental and modelling research is required to support this claim.

In the pilot-scale EAF measurements of Papers I and II, it is noted that the slag composition has a significant effect on the optical emissions and plasma analysis, with arc-slag and arc-steel interactions. These measurements provide a good basis for industrial experiments in which e.g. the images of the arc cannot be recorded.

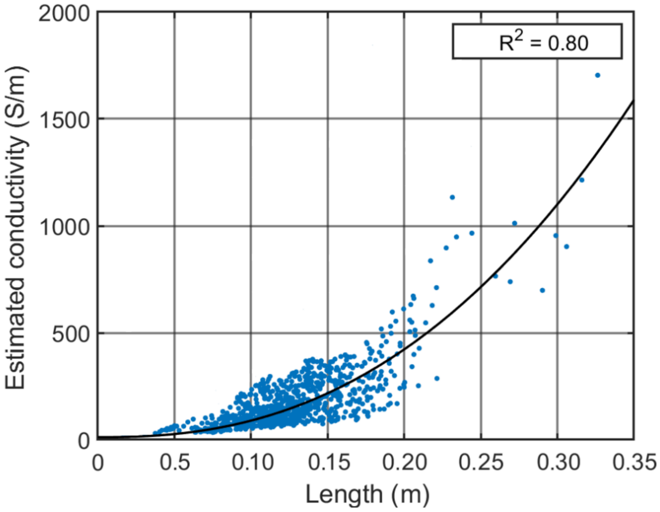

Figure 5.9: Estimated conductivity with increasing arc length for 0.03–0.05 m of the arc [Paper II, reprinted under the CC BY 4.0 license].

In industrial furnaces, the arc length can be indirectly estimated from the voltage values of the furnace, with which the voltage gradients and conductivity could also be evaluated. Furthermore, based on these results, a general estimate of the slag composition could be measured when the electrode is in contact with the slag. Once the slag composition is known, the effect of slag on these parameters can also be analysed more deeply. In the best-case scenario, the slag composition would be measured online with OES. OES could also determine the interactions between the arc, slag, and steel.

5.3 Industrial EAF spectrum and plasma analysis

The measurement campaign at an industrial EAF was conducted at Deutsche Edelstahlwerke in Germany and lasted several weeks. A hole through which the measurement head looked into the furnace was prepared in the furnace roof, according to careful planning for the best view cone into the arc. The measurement head was welded to the furnace roof. The steel grades consisted of both high alloyed and carbon grades. Schematics of the measurement set-up and the EAF are presented in Figure 4.5.

The emission spectra from the NIR spectrometer were divided into 9 wavelength ranges, centred at 570, 650, 700, 750, 800, 850, 910, 970, and 1,000 nm, to which Gaussian functions were fitted so that the convolution of the fits covered the whole spectrum. The FWHM values of the Gaussians were very high between 20 and 60 nm, because the purpose was to cover the spectral range from 500 to 1,000 nm. The NIR spectra cover the visible and infrared light, which contains part of the thermal radiation.

The intensity distribution of the high alloyed and carbon steel grades are compared in Figure 5.10. Both high alloyed and carbon steel grades consist of two melts in Figure 5.10. The distribution of the intensities shows that high alloyed steel grade had more high intensity spectra in the near-infrared region, meaning the heat radiation was higher for the high alloyed steel compared with the carbon steel grade. The time-evolution of the spectra also show that during the foaming practice, the spectrum intensity decreased in all wavelength ranges, an indication of lower energy losses via radiation.

The time-evolution of the intensity distribution for 570, 750, and 910 nm-centred fits and estimation of the molten bath temperature are presented in Figure 5.11 a and b for high alloyed and carbon steel grades respectively. The molten metal bath temperature has been estimated from the OES spectra, using Equation (2.4). Both these analyses provide valuable information about the processes inside the furnace. As can be seen from Figure 5.11 a, the intensity drops between times 100 and 200, whereas the estimated temperature increases. The same can be observed for the carbon steel grade at between times 200 and 300, where the intensity drops, but

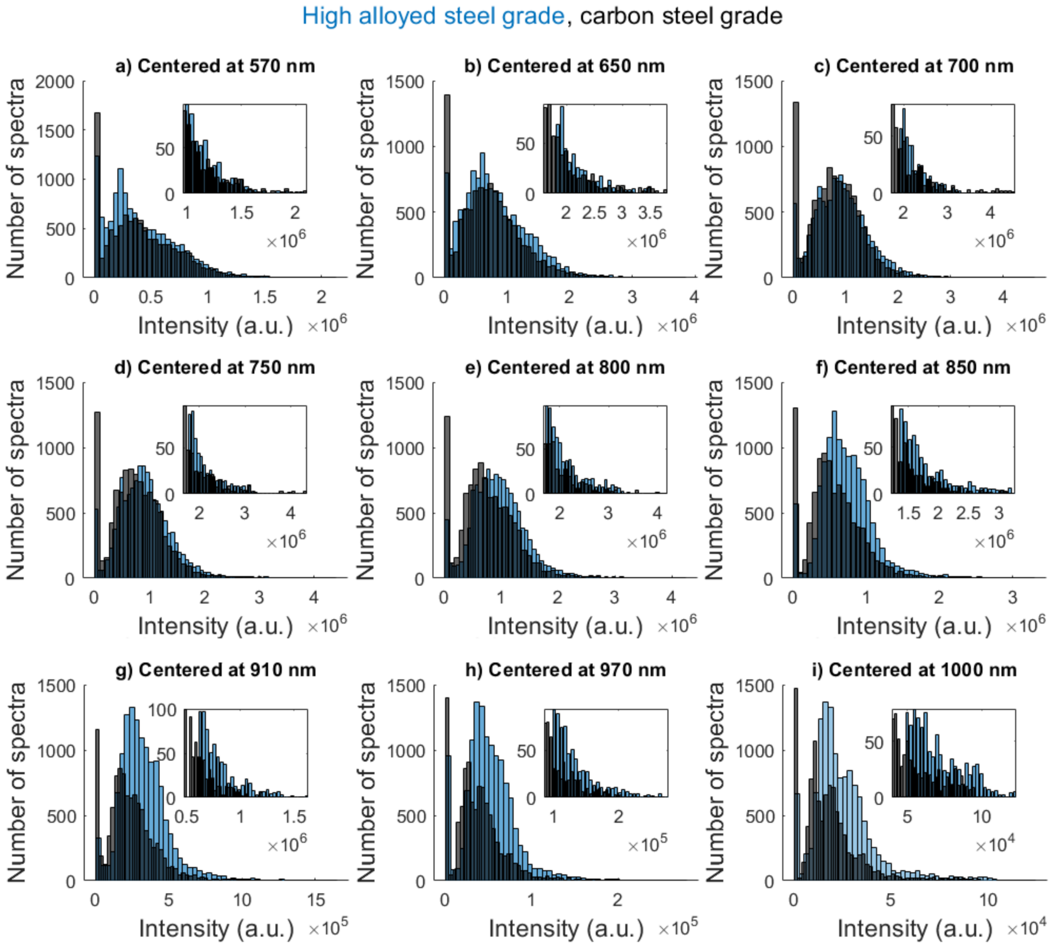

Figure 5.10: Intensity distributions of a) 570 nm, b) 650 nm, c) 700 nm, d) 750 nm, e) 800 nm, f) 850 nm, g) 910 nm, h) 970 nm, and i) 1,000 nm for high alloyed and carbon steel grades. Both grades consist of two melts. The magnifications in each graph display the intensities with fewer than 100 counts [Paper III, reprinted under the CC BY 4.0 license].

the temperature remains relatively constant. If it is observed e.g. during foaming practice that the near-infrared intensity has increased, this could be used as an indication that the foaming has not worked properly, because the energy loss via radiation would remain unaffected. This analysis is further supported by the molten bath temperature analysis, because it can be used to estimate the molten bath surface or the foam temperature.

However, the estimated temperatures followed intensity trends between 320–470 times and 100–200 times for high alloyed and carbon steel grades respectively. For the carbon steel grade, this time range was associated with foaming, which means that

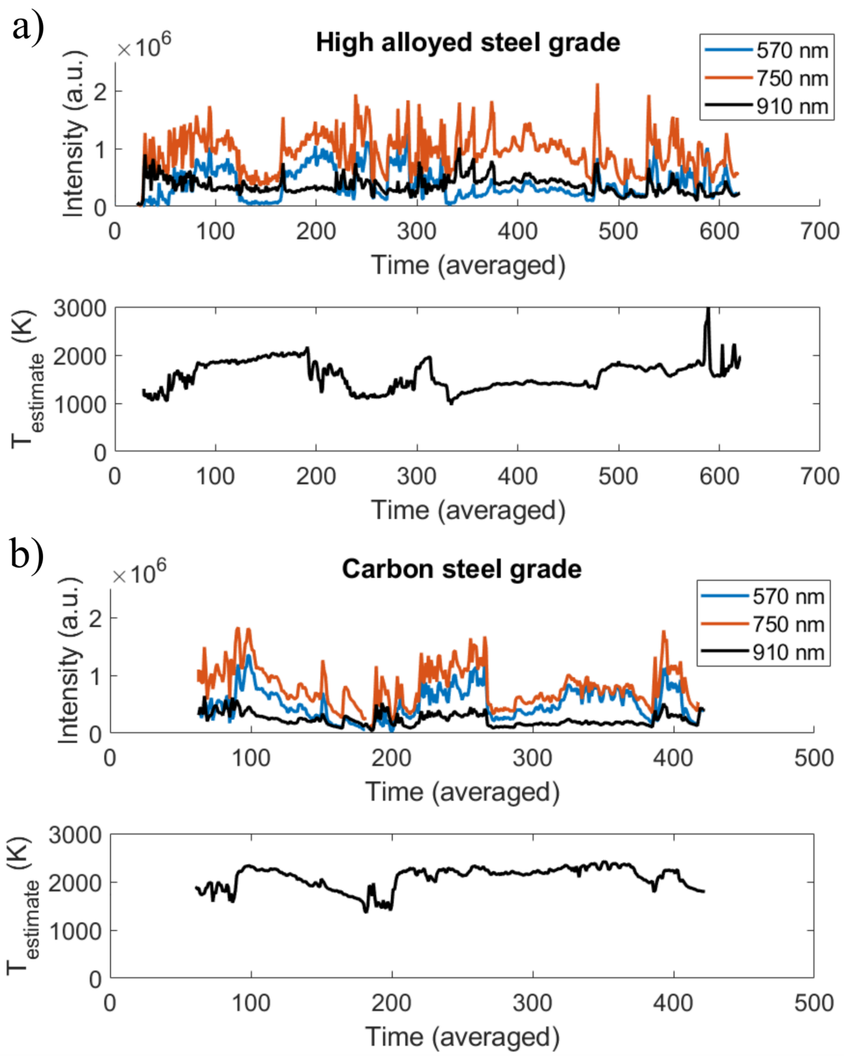

Figure 5.11: Time-evolution of the intensity distribution and estimate of the molten bath temperature for a) high alloyed and b) carbon steel grade. The data has been averaged over five spectra [Paper III, reprinted under the CC BY 4.0 license].

the foaming practice lowered the molten bath surface temperature and reduced heat losses via radiation. The intensity and temperature time-evolution can be measured online, which makes this method a viable tool to study the foaming practice and radiative properties of the molten bath. The high temperature peaks for high alloyed steel around time 600 correspond to the arc spectra. Equation (2.4) does not hold when the arc is in the view cone of the measurement head, because the temperature exceeds 5,000 K, and the spectrum is highly influenced by the atomic and molecular optical emissions.

The electric arc was visible only for the high alloyed steel grades within 30 mins before tapping for 70% of the melts. According to the plasma diagnostics, the best spectra were observed 5–20 mins before tapping. These time periods before the tapping would be optimal to determine the slag composition with OES, because at this point, the melt has had time to mix, and the slag represents its final composition. However, 5 mins before the tapping might be too late for process optimisation or alloying element additions. The visibility of the arc is unique for each measurement set-up and steel plant, so the time range within 30 minutes before the tapping might not apply to other furnaces. There are ways to improve the arc visibility, such as increasing the arc length and optimising the view cone into the furnace, which can be utilised in different EAFs, depending on the structure of the furnace.

The plasma temperatures were determined with 5 Cr I, 7 Fe I, and 4 Ca I emission lines. A comparison of these temperatures showed that Cr I and Fe I temperatures agreed with each other more frequently than those of Ca I, which fluctuated considerably. Differences in the plasma temperatures from different elements indicated that the plasma was not always in the LTE, despite the fact that the electron density exceeded the LTE criterion density [19]. The plasma temperatures tended to converge towards the end of the melt, indicating better LTE conditions. The plasma diagnostics also illustrated some cases in which the quality of the spectra was poor; hence, caution should be exercised in using such spectra e.g. for slag composition analysis. An example of the time-evolution of the plasma parameters before the end of the melt is presented in Figure 5.12.

The time-evolution of the plasma parameters of Figure 5.12 demonstrate how the

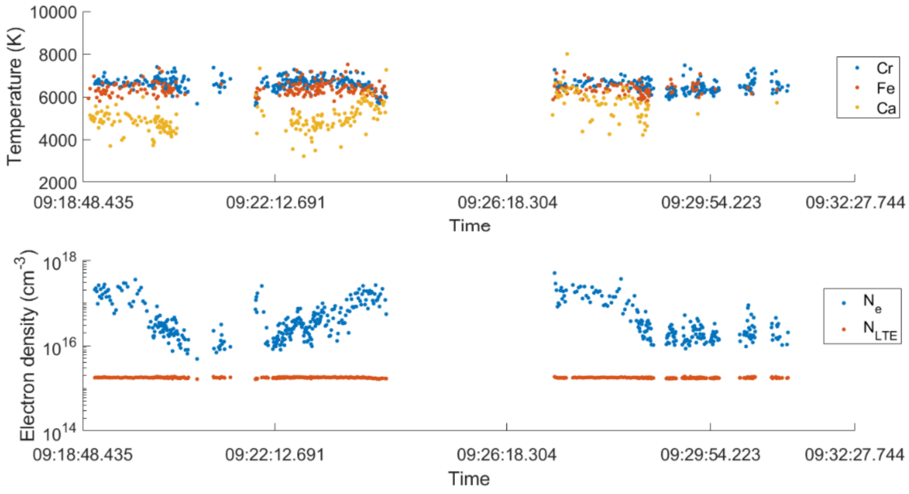

Figure 5.12: Time-evolution of the plasma temperatures, electron density, and LTE criterion density. The melt ends at 09:37:40 [Paper III, reprinted under the CC BY 4.0 license].

plasma analysis can be used to estimate the quality of the spectra. demonstrate how the plasma analysis can be used to estimate the quality of the spectra. The electron densities have been observed to exceed the LTE criterion density, but the plasma temperatures may show large differences between each other, causing a deviation from the LTE. Another reason for the differences in the plasma temperatures may be that the optical emissions occur at different locations within the plasma. In Figure 5.12, iron and chromium optical emissions originate closer to the core in comparison with the calcium. Since the temperature is the highest in the core of the arc, this would cause a temperature difference for the particles that reside in different sections of the plasma.

For the carbon steel grade, the arc was momentarily visible only in the ignition of the arcs, when the arc lengths may have been long and the arcs wandered on the charge material. Hence, carbon steel grade requires special procedures to be implemented for the arc to be seen later in the process. An example would be increasing the arc length momentarily for a better view of the arc. The view cone to the arc is very affected by the foamy slag, which is a common practice for carbon steel grades and can at least partially cover the arcs. Another issue to be considered concerning the visibility of the arc is whether the batch sizes change significantly. Different batch sizes can result in a varying melt surface height, which in turn affects how well the arc is seen. This aspect could also be problematic for high alloyed steel grade batches.

To overcome poor visibility of the arc and control the instances when the arc is in the view cone of the measurement head, the operator would need to implement additional procedures during the melting. Before these procedures are executed, it is important to ensure that both the view cone and aperture of the fibres are optimised and well aligned. There can be significant differences between each furnace, and thus these aspects must be considered separately for each campaign.

However, it has been demonstrated that the spectrum intensities and molten bath surface temperatures can be analysed throughout the measurement period. The most promising applications of these analyses are optimising the charging of additional raw material baskets or alloying elements into the furnace, and monitoring the foaming. As the charge material melts, more and more light reaches the spectrometer, which can be used to evaluate the meltdown of the solid material in the furnace. The example in Figure 5.11 demonstrates how the intensities and estimated molten bath surface temperatures behave during the EAF procedures, and how they can be used for process control.

5.4 LF slag composition analysis with OES

The measurement campaign at the industrial LF was conducted at Deutsche Edelstahlwerke in Germany and lasted several weeks. The measurement head was located 5 m from the furnace, and no special procedures were therefore required to shield the measurement head from damage. However, a pressurised airflow was used to ensure that no slag splashes reached the measurement head. The measurement head was connected to a manipulator that allowed vertical adjustment and the angle of the measurement head to be changed.

An example of the line ratio analysis is presented in Figure 5.13. The number of melts in the emission line ratio analysis varied between 20 and 60 melts, depending on the spectrometer in question. UV spectra were much scarcer than VIS and NIR, and the NIR spectra were the most abundant. A light gathering lens was required for the UV spectrometer for sufficient data acquisition. No emission lines were detected below 300 nm. The UV light was efficiently absorbed by the furnace atmosphere, which is one reason for the poor light acquisition in the UV range.

Ten Ca I, 1 Ca II, seven Mg I, and one Mn I lines were found to show potential for evaluating the relation between the XRF and OES analyses. These lines are presented in Table 5.1. Line ratios were studied instead of plain emission line intensities to

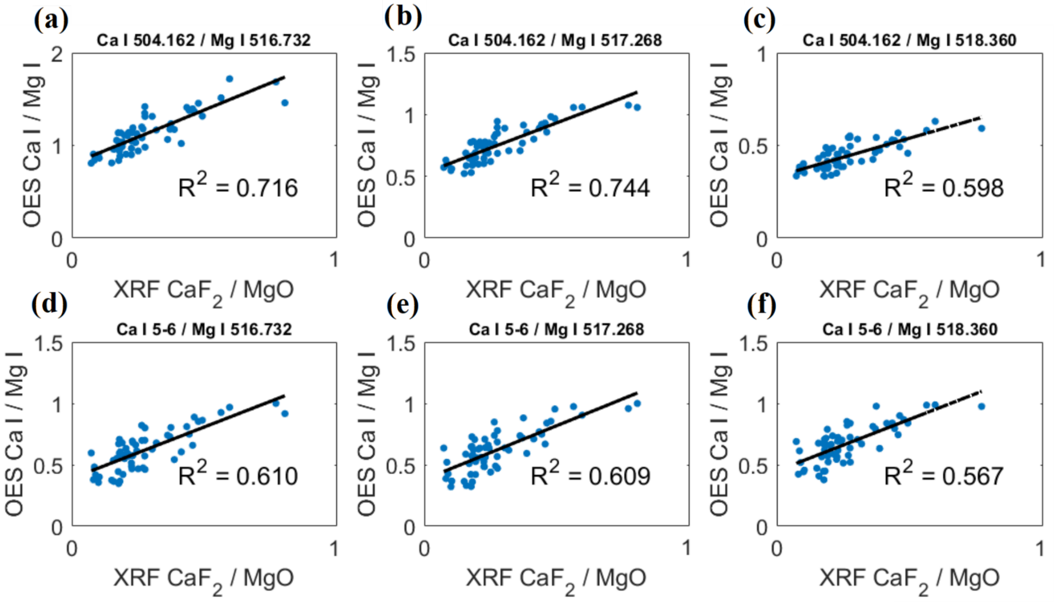

Figure 5.13: Emission line ratios for Ca I / Mg I correlated with CaF_2 / MgO for NIR spectra. 60 melts were used in (a), (b), (d), and (e), whereas (c) and (f) have 59 melts. The calcium line numbers refer to the # in Table 5.1, and the XRF axes have been normalized [Paper IV, reprinted by permission of ISIJ International].

Table 5.1: Emission lines that were used to correlate OES data with XRF in the LF campaign [Modified from Paper IV, reprinted by permission of ISIJ International].

Species	#	Wavelength (nm)	UV	VIS	NIR
Ca I	1	387.578	x		
	2	395.705	x		
	3	397.371	x		
	4	504.162		x	x
	5	526.424			x
	6	527.036			x
	7	558.197		x	
	8	558.876		x	
	9	559.447		x	
	10	560.285		x	
Ca II	1	409.719	x		
Mg I	1	382.935	x		
	2	383.230	x		
	3	383.829	x		
	4	392.647	x		
	5	516.732		x	x
	6	517.268		x	x
	7	518.360		x	x
Mn I	1	403.076	x		

remove the effect of the changing spectrum intensities. The R^2 of the relations between the XRF and OES was between 0.57 and 0.74, which is relatively low due to the harsh environment of the furnace, which affects the spectra. To improve the correlation, more sensitive spectrometers could be used and the position of the measurement head could be changed. Positioning nearer the furnace could improve the view cone of the measurement head and hence yield better spectra. A potential placement in addition to the roof the furnace would be the slag door of the furnace vessel.

Ca I plasma temperature with four Ca I lines was found to have a non-linear relation with the CaF_2 content of the slag. This relation is illustrated in Figure 5.14. The relation includes 78 melts with $R^2 = 0.81$, hence yielding a better relation than the line ratio analyses. It can be assumed that other slag components would also show similar relationships with the plasma temperatures derived from their atomic counterparts. The abundance of emission lines in the EAF and LF OES spectra, however, limits the number of emission lines that can be used for plasma analysis due to overlapping lines. The FWHM values of the emission lines have been observed to be higher in industrial than in pilot-scale furnaces, which is probably caused by the harsher conditions inside the furnaces. Using more sensitive spectrometers and repositioning the measurement head could be implemented to improve the quality of the spectra.

HSC Chemistry software was used to determine the decomposition pathways of

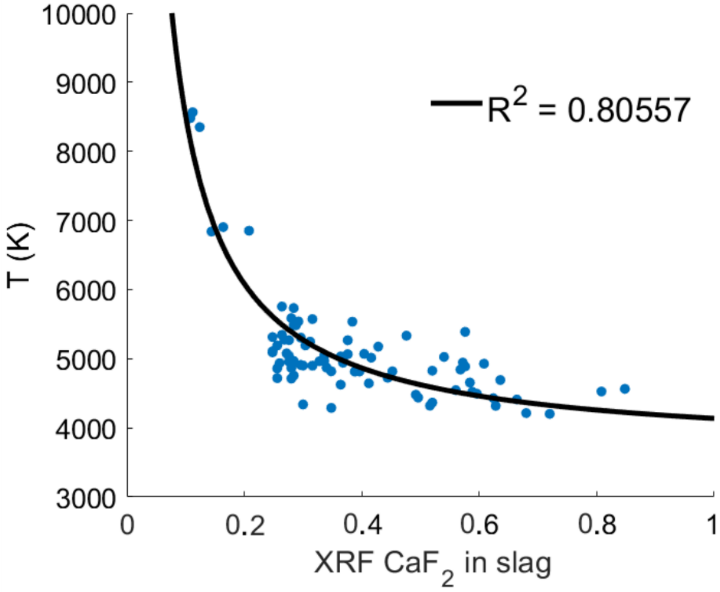

Figure 5.14: The non-linear relation between the Ca I plasma temperature and the XRF-analysed CaF_2 slag content. The XRF axis has been normalised [Paper IV, reprinted by permission of ISIJ International].

several molecular slag components with respect to increasing plasma temperature. These results are displayed in Figure 5.15. The slag components, excluding SiO, were found to be mostly in their atomic form already at a plasma temperature of 5,000 K. The most persistent molecules around 5,000 K were SiO and CaF, with minor amounts of CaO and AlO. Temperatures below 5,000 K represented the edges of the plasma, where the plasma also contained some molecular species. This means it could be expected that the emission spectra also contained molecular emission bands from slag components, provided that the energy of the plasma was sufficiently high to excite these molecules at the edges of the plasma. The effect of the changing amount of CaF_2 and MgO in the slag was studied at plasma temperatures of 5,000 and 10,000 K to identify how the Ca I, Ca II, and Mg I content in the plasma was affected by these changes. At 5,000 K, increasing the CaF_2 content of the slag resulted in a slightly non-linear relation between the Ca I atoms in the plasma and the CaF_2 content, whereas Ca II and Mg I had linear relations with increasing CaF_2 and MgO slag content respectively. At 10,000 K, Ca I, Ca II, and Mg I had a linear relation to the increasing CaF_2 and MgO content. However, the number of Mg I atoms in the plasma changed only negligibly between 5,000 and 10,000 K, which means that the neutral atomic magnesium content of the plasma remained relatively stable with the changing plasma temperature. This makes Mg I lines good reference lines for the line ratio analysis.

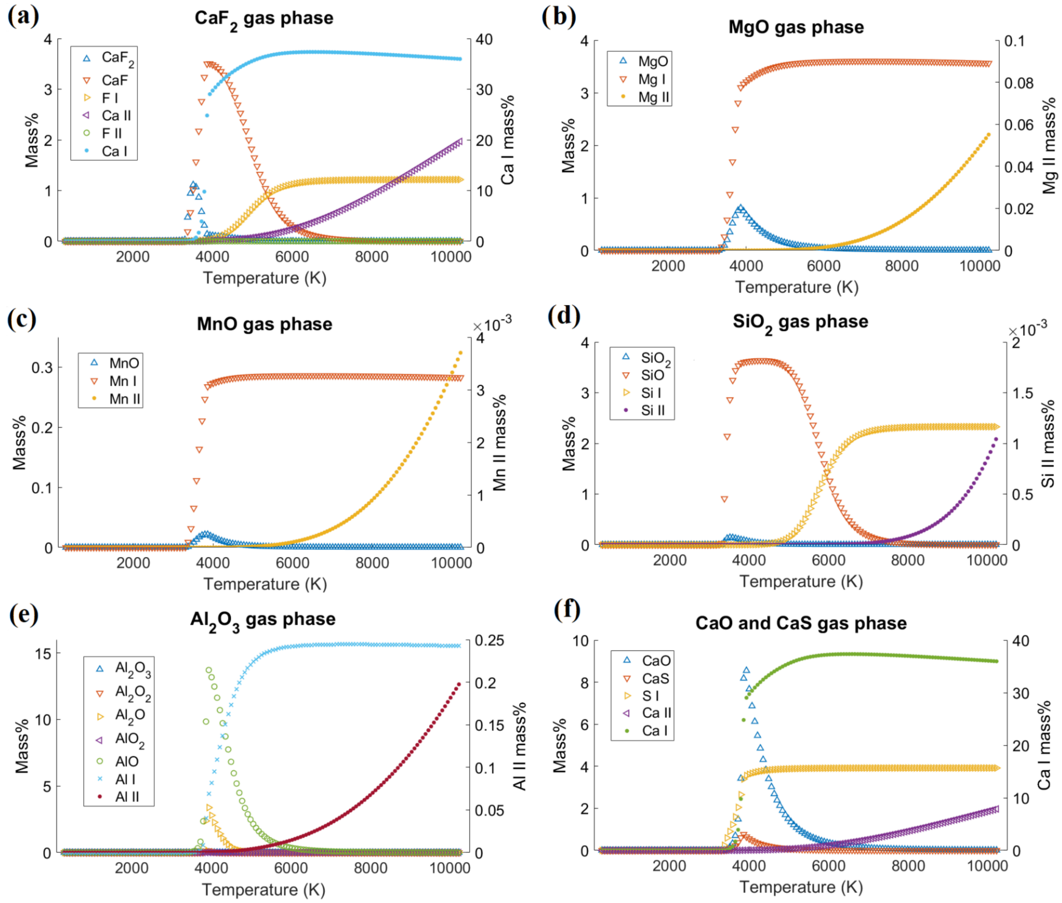

Figure 5.15: HSC chemistry phase transition computation results for the most common LF slag components [Paper IV, reprinted by permission of ISIJ International].

With the results from the LF campaign, OES shows potential for an online slag composition analysis tool for the ladle treatment. However, the measurement set-up requires further optimisation to improve the light acquisition from the arc. This could be achieved by changing the measurement head alignment or choosing a more optimal position. Since the places that are suitable for the positioning of the measurement head are limited in an industrial plant, the quality of the spectra could be enhanced with more sensitive spectrometers. To obtain OES data from all the heats, the slag wall that accumulates on the ladle should also be crushed before the ladle treatment.

5.5 Prospects of online analyses with OES

OES is a viable solution for online analysis, because the data can be acquired in real time, the spectrum analysis can be optimised for fast performance, and the data validation can be done jointly with the general spectrum analysis. The results from the industrial EAF and LF demonstrate the significant differences between these two furnace types and how they affect the measurement set-up, data acquisition, and processes that can be monitored with OES. Hence, OES as an online analysis method has been discussed individually for the EAF and LF.

5.5.1 EAF

In terms of the arc's visibility, the high alloyed steel grade is expected to present a much easier case than the carbon steel grade. The industrial trials showed that high-quality arc emission spectra were observable for the high alloyed steel grade, whereas the arc was not observed for the carbon steel grade. The carbon steel grade would probably require additional practices such as momentarily increasing the arc length for better arc visibility. This could be implemented at some point towards the end of the melt, when the charge has melted and the molten bath has had time to mix.

The atomic emissions include several intensive lines from Ca I, Ca II, Mg I, Cr I, Mn I, and Fe I. These lines are relatively isolated or easily deconvoluted. Al I and Si I species would require more sensitive measurement equipment, because intensive emission lines for these elements reside in the UV range, which has proven difficult to measure in the industrial environment. Some of the F I and S I emission lines, however, reside in the visible light range, but distinguishable emission lines from these species were not detected in the pilot-scale or industrial furnace spectra.

Plasma diagnostics offer a good validation tool for the arc spectrum quality, because it can be used to assess the fulfilment of the LTE. Furthermore, electron density states the approximate amount of charge carriers in the plasma, which means that the conductivity of the arc can also be evaluated. The plasma temperature from Ca I emission lines was found to be related to the CaF_2 content of slag in the LF campaign, which means that similar relations could also be found for the EAF.

Since the arc was visible only towards the end of the melt for the high alloyed steel grade, the plasma diagnostics and slag composition analyses cannot be used throughout the measurements. Operating with long arcs the whole time would increase the arc visibility, but it is not energy efficient to operate with long arcs for a long time. Furthermore, longer arcs heat up a larger volume of the atmosphere compared to shorter arcs [54], which results in heat loss and could even expose the furnace lining to heat damage. However, although the arc would not be visible until towards the end of the melt, the OES spectra can be used to observe the melting of the charge material and estimate the surface temperature of the molten bath. This information could be used e.g. to adjust the instance for the charging of the second basket of raw material and to monitor the foaming conditions.

The measurement equipment has been proven to withstand the harsh conditions of the furnace when the measurement head is welded to the EAF roof. An external stimulus for the optical emissions is not required, because the arc plasma has suitable conditions for optical emissions. Hence, the measurement set-up requires only proper aiming and alignment of the view cone. Once well installed, the measurement equipment requires no additional maintenance. The spectrometer cabinet can be accessed between melting processes, and the data storage computer can be located in the operator room. If the measurement head is welded to the furnace roof, it is the only component that needs proper cooling and protection from slag splashes. If required, the measurement head can be adjusted or repaired during the regular maintenance of the furnace.

5.5.2 LF

In the case of the LF, the measurement head can be located several metres from the furnace if there is an opening between the ladle and the roof. This brings its own advantages and disadvantages, because the equipment is safely away from the furnace atmosphere, but the location of the measurement head must be carefully considered to enable a good view into the furnace. Welding the head to the roof also presents challenges, because it is a permanent solution for a measurement campaign. Furthermore, the roof may not have a suitable place for the head to welded into due to e.g. the positioning of the cooling panels.

Generally, the LF is an easier measurement environment than the EAF. When the OES analysis was compared with the XRF analysis, it showed that OES was a potential tool for LF slag composition analysis, especially for the CaF_2, MgO, and MnO content. Similar atomic emissions from slag components have been identified for the LF compared with the EAF. During the campaign, it was noted that a light gathering lens significantly increased the light acquisition in the UV range, which made it possible to analyse the emission lines in lower wavelengths as well. With an optimal view cone and measurement head position, Al I would also be analysable from the UV with a lens around 390 nm. However, the most prominent Si I lines are below 300 nm, which would require a more sensitive spectrometer.

The plasma diagnostics are also applicable to the LF data for arc spectrum quality evaluation. In addition, a relation between the Ca I plasma temperature and CaF_2 was determined from the industrial LF campaign. With more measurement data, it is expected that similar relations with plasma temperatures from other atomic species would correlate with corresponding slag components.

The slag composition analysis will probably have more impact on ladle treatment than on the EAF. Since there is no solid charge material in the ladle furnace, the visibility of the arc is much better than in the EAF. Arc spectra can therefore be acquired in almost any ladle treatment process step, whereas in the EAF, the arc spectra were observed to be observable within the last 30 minutes before tapping and for the high alloyed steel grade.

The intensity distribution and estimation of the molten bath surface temperature determined for the industrial EAF spectra can also be determined for the LF spectra. However, since the arc was very frequently in the view cone of the spectrometers in the LF campaign, the temperature evaluation does not hold under the approximation that the observed temperatures are less than 5,000 K. The intensity distribution is also more difficult to evaluate, because the arc significantly affects the overall spectra. If it is important to measure the intensity distribution and the molten bath surface temperature, a spectrometer can be focused outside the movement range of the arc to observe only the molten bath surface. Furthermore, a specific region of the molten bath surface can be selected for the intensity distribution and bath temperature analysis, because the aperture and alignment of the measurement head can be changed and adjusted.

Chapter 6

Industrial relevance

6.1 Slag composition analysis

Online analyses and modelling have received considerable interest from the steel industry due to their direct effect on efficient resource usage, timing of adjustments to optimise steel composition, and identification of unusual process conditions and hazardous events. With currently used slag composition analysis methods such as XRF, it is possible to determine the slag composition only after careful sample preparation. The slag composition information cannot be used directly to modify the batch from which the slag sample was taken, but it can be used to anticipate the future progress of the process for the subsequent melts.

The importance of online slag composition analysis is evident for the steel industry because slag composition affects chromium recovery [55, 56], slag foaming [1, 29–32, 56], inclusion characteristics [57–59], and dissolution of MgO and refractory lifetime [28, 60, 61] to name but a few. With online analysis, these aspects could be monitored during the melting, which would enable the operator to react to the changing properties of the slag. The problems of online analysis methods in industrial furnaces arise from the extreme environment of the furnace due to high temperatures, the harsh atmosphere, and the limited view into the furnace. Most of the promising methods for online analyses cannot withstand these conditions, would require frequent and extensive maintenance, or would not respond to the changing environment inside the furnace.

Online slag composition analysis methods are important research topics because of slag's effect on the chemistry and phenomena in the furnace and on steel composition. With e.g. poor basicity values, the slag may dissolve the refractory lining, or impurities from the slag may transfer to the steel, forming harmful inclusions. With online slag composition analysis, the furnace operator can assess the slag properties in real time and adjust the material additions to optimal amounts and instances. The role of slag chemistry is crucial in LF treatment, which is practically the last opportunity to affect the composition of the final steel product. With optimised LF treatment, harmful inclusions can be removed, valuable material can be retrieved from the slag for the steel, and slag properties can be modified for optimal slag-steel interaction.

From the industrial perspective, the most promising aspect of OES is online slag composition analysis. For example, the chromium and iron content of slag are of interest due to their value for steelmaking. It is important to minimise the amount of these materials in the slag and valuable alloying elements as much as possible. Another component that needs to be monitored is the magnesium in the slag, because it is usually dissolved from the furnace lining into the slag. The simplest scenario of OES as a slag composition analysis tool would be to monitor the iron, chromium, and magnesium content of the slag, allowing the furnace operator to optimise slag composition to minimise both iron and chromium losses, and prevent MgO dissolving from the lining into the slag.

6.2 Molten bath temperature and radiative heat transfer

The molten bath surface temperature can be evaluated throughout the melting process. The thermal curve of the OES spectra contains information about the temperature of the measured object, which can be selected when aiming the measurement head. If bath temperature analysis is the priority, the optical fibres can be aimed at specific locations on the bath surface. However, when using several spectrometers, one spectrometer can be aimed at the slag surface and the others at the electric arc for plasma and slag composition analyses. By aiming the spectrometers at different locations, the radiative heat transfer of both the molten bath and the electric arc can be evaluated. This information would be valuable especially during foaming practice, when heat losses should be minimised.

6.3 Plasma diagnostics

The plasma diagnostics can be used as a data validation tool for OES spectra. Additionally, information about the arc plasma can provide an estimate of the amount of metal vapour, the number of charge carriers, and the distribution of atomic and molecular species in the plasma. The time-evolution of plasma parameters, such as plasma temperature and electron density, can be used to monitor the changes that arise due to e.g. lengthening of the arc, foaming of the slag, and material additions. The fluctuations of the plasma parameters also depict the changes in the furnace atmosphere, because different emission lines react differently to changes in the atmosphere. However, if the plasma parameters fluctuate significantly, it may also indicate that the arc movement on the slag surface is very erratic, and the arc is wandering around the slag. The plasma temperatures from individual elements may also be related to the slag content of the corresponding slag component, as demonstrated in Paper IV.

6.4 Other application possibilities of OES in EAFs and LFs

The bases of OES spectrum analysis, arc spectrum plasma diagnostics, changes in the intensity distribution, and molten bath temperature evaluation were established in Papers I, III, and IV. However, OES is not limited to these analyses, which deal mainly with atomic emissions from the slag components and general properties of the spectra. Promising aspects of OES applications for EAFs and LFs are especially the evaluation of the gas content of the atmosphere and the detection of molecular emissions from both the gas and slag particles. In this section, this analysis potential is discussed with the spectra that were recorded in the experiments of this thesis.

6.4.1 Off-gas composition analysis with OES

The gases in the furnace atmosphere can significantly affect the OES spectra, because they can increase the optical thickness of the atmosphere and absorb the optical emissions from the arc. Consequently, a very harsh atmosphere could hinder the accuracy and reliability of the arc spectrum analysis. This is most notable during the meltdown of the charge material in the EAF, when gas evaporation from the melting materials is high.

However, the absorption or optical emissions from the gas particles can provide useful information, because they are related to the amount of gases in the furnace atmosphere. A common practice in furnaces is to have an off-gas analysis system, which monitors the CO_2, CO, C_2, H_2O, O_2, and even H_2 content of the atmosphere. For example, with this analysis, an abnormal increase in the water content could be detected, and further damage to the water-cooling system can be prevented.

Figure 6.1 displays five NIR spectra from the different process stages of the pilot-scale EAF. The spectrum at arc ignition, when the arc is not yet completely in the view cone of the measurement head, displays several atomic emission lines for O I, C I, H I, and N I with Na I, K I, and Li I. Just after ignition, when the arc comes to the view cone of the measurement head, the slag component emission lines can be observed. As the melting continues, the spectrum characteristics also change, as can be seen from the 2.5-min, 5-min, and 10-min spectra after ignition. However, there is no specific route by which the spectra evolve, because the position of the arc, slag homogeneity, and atmosphere affect them. Hence, the spectra always represent the momentary situation inside the furnace, and can vary in quality and character.

In the pilot-scale EAF, the O I, N I, H I, and C I emission lines can be observed throughout the melting process when the arc is in the view cone of the measurement head. The oxygen, nitrogen, hydrogen, and carbon can be assumed to originate mainly in the atmosphere. However, some of the gases may arise from the molten bath surface due to e.g. foaming or oxygen lancing. The presence of these atmospheric components means that OES is a viable tool to estimate the composition of the atmosphere, i.e. to provide an alternative solution for off-gas analysis. Off-gas analysis can be performed simultaneously with plasma diagnostics and slag composition evaluation, because it only requires fitting of the emission lines for O I, N I, H I, and C I. However, if the number of fitted emission lines increases significantly, the computation time will increase. This must be taken into account in an online application.

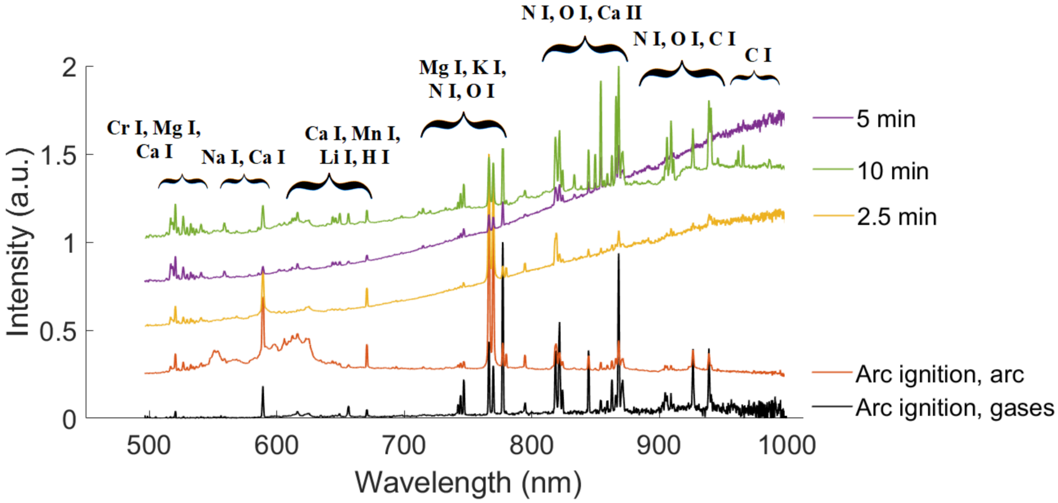

Figure 6.1: NIR emission spectra at arc ignition and 2.5 min, 5 min, and 10 min after ignition from the pilot-scale EAF. The intensities have been normalised, and the spectra are separated from each other by y-axis scaling.

6.4.2 Molecular optical emissions

It was occasionally noted during the pilot-scale and industrial furnace measurements that the OES spectra contained molecular emissions in various process steps. Since the high energy of the arc dissociates most of the molecular compounds, as demonstrated in Figure 5.15 for the LF slag components, the molecular emissions probably originate at the edges of the plasma column, where the plasma temperature is lower than in the core. Furthermore, molecular recombination of the atomic species can provide optical emission from the molecules that are formed from these atoms.

For example, the broad molecular optical emissions from CN can be observed in the UV spectra of Figure 2.3 between 370 and 390 nm. Optical emissions from the CN molecule have also been observed in microwave plasmas [62], ethylene-airflow-plasma [63], glow discharges [64], laser-induced breakdown spectroscopy (LIBS) study of solid samples [65], and laser ablation studies [66]. Several formation routes of CN at combustion temperatures have been reviewed by Dagaut *et al.* [67], involving reactions between e.g. C_2, N_2, C, and CH. Some analyses have related NO to the formation of cyanide (CN) by reacting with C and CH [68]. Formation of CN can also involve hydrogen cyanide (HCN) reacting with OH and producing CN and H_2O [69].

In the single-pulse LIBS work of Gaft *et al.* [70] molecular band emissions from CaF were observed around 532, 584, 603, and 623 nm and from CaO around 550, 615, and 623 nm. Since majority of the CaF_2 and CaO have dissociated to their atomic components around 5000 K, as demonstrated in Figure 5.15, the origin of these emissions could be the outer edges of the plasma, where the plasma temperature is lower. However, this analysis is beyond the scope of this thesis.

In addition to pilot-scale and industrial furnace measurements, Mäkinen *et al.* [71] measured laboratory EAF spectra in a range from 200 to 600 nm for various slag components. In these spectra, they recorded faint AlO band emissions between 450 and 500 nm, with a C_2 Swan band around 470, 515, and 560 nm. It is very probable that the AlO emission bands will be very difficult to identify from the spectra due to the high background radiation in industrial furnaces, whereas the C_2 Swan bands have occasionally been observed in the research of this thesis. Mäkinen *et al.* attributed the origin of the C_2 Swan band to the carbon that is evaporated from the graphite electrodes. This raises a new and interesting possibility of using OES to monitor the consumption of the electrode material online. Since the position of the electrodes is well known during the EAF and LF processes, the spectrometer could be aimed at the electrode to gather the C_2 emissions from the electrode. However, this procedure still requires industrial measurement campaigns to be validated.

Chapter 7

Summary

The main results of this thesis are:

1. Arc characteristics and electrical parameters are significantly influenced by slag composition
2. Plasma analysis is a viable tool for studying the properties of the arc and evaluating the quality of the spectra
3. Online OES data from the arc in an industrial EAF would be available within 30 min before tapping for high alloyed steel grade
4. Carbon steel grades in an industrial EAF require special procedures for the arc to be visible due to foaming slag practice
5. The OES spectra can be used online to monitor the melting of the charge material and radiative heat transfer, and to estimate the temperature of the molten bath
6. The CaF_2, MgO, and MnO content of the slag can be evaluated in the industrial LF with OES and plasma diagnostics
7. Most of the molecular slag components are in their atomic counterparts at plasma temperatures exceeding 5,000 K

The work of this thesis covers arc characterisation in a pilot-scale EAF with OES, combined with image analysis and measurement campaigns in the industrial EAF and LF. OES has been found to be a promising data analysis tool for electric furnaces due to online data acquisition, fast spectrum analysis with emission line fitting and plasma diagnostics, and simple measurement equipment. The required equipment allows flexible adjustments, either by welding the measurement head to the furnace roof or positioning it several metres from the furnace. In the EAF, the roof covers the view into the furnace, and the measurement head therefore needs to be welded to the roof with a view into the furnace. A pressurised airflow is a sufficient precaution to prevent the slag splashes from reaching the measurement head and to cool it down.

The spectrum information, arc visibility, plasma diagnostics, image and OES analyses, and results of this thesis are presented in Table 7.1. The pilot-scale EAF measurements highlighted the prospects of OES analysis for EAFs and LFs through characterisation of the arc, testing of the applied methods, and acting as a basis for the improvement and extension of industrial applications. The properties of the arc and the electrical data of the furnace have been related to the slag composition, which is the fundamental aspect that originally prompted this research. Since all the observed emission lines cannot be fitted due to the limited computation time in online analysis, careful identification and selection of the most prominent emission lines are necessary. With the pilot-scale analysis, suitable emission lines for the major slag components were identified. The analysis was further developed with plasma analytics as a data validation tool for the spectra. OES combined with the plasma analytics acts as a strong basis for an industrially viable online analysis method.

The industrial OES measurement campaigns assessed both the advantages and

Table 7.1: Summary of the results. T_{plasma} is the plasma temperature, N_e is the electron density, and N_{LTE} is the LTE criterion density.

	Pilot-scale EAF	Industrial EAF	Industrial LF
UV spectra	High-quality	Low intensity, requires lens	Low intensity, requires lens
VIS spectra	High-quality	Medium-quality	Medium-quality
NIR spectra	High-quality	High-quality	High-quality
Arc visibility	Good in all process steps	High-alloyed steel: good before tapping Carbon steel: low	High-alloyed steel: good Carbon steel: good
Future improvements	Trying different camera filters	Arc lengthening for better arc visibility	More sensitive spectrometers
T_{plasma} (K)	4,500 - 9,100	3,000 - 9,000	4,000 - 9,000
N_e (cm^{-3})	3.6×10^{16} - 4.1×10^{20}	7.0×10^{15} - 4.0×10^{17}	1.7×10^{18} - 7.0×10^{19}
N_{LTE} (cm^{-3})	1.3×10^{15} - 3.4×10^{15}	1.7×10^{15} - 1.8×10^{15}	1.2×10^{15} - 2.0×10^{15}
Arc image analysis	Length, diameter, brightness, area, and position	Not viable	Not viable
OES slag analysis	Not determined in this thesis	Possible, but requires more validation and industrial data	Ca I, Ca II, Mg I, and Mn I related to CaF_2, MgO, and MnO
Other results	Effect of the slag composition on the length-voltage relation of the arc	Estimate of the molten bath temperature and radiative heat transfer from the spectra	Relation between Ca I plasma temperature and CaF_2 slag content

limitations of OES in industrial EAFs and LFs. The advantages for both the EAF and LF were identified as online data acquisition, flexible analysis methods ranging from slag composition and plasma analyses to the molten bath temperature evaluation, and a negligible maintenance requirement. It was noted in the industrial EAF campaign that the electric arc visibility differed greatly for the high alloyed and carbon steel grades, for which the arc could be observed only for the high alloyed steel grades. The poor visibility of the arc for carbon steel grade was attributed to the foaming slag, which is a common practice for carbon steel grades. However, the arc could be brought to the view cone of the spectrometer by e.g. lengthening the arc momentarily. In the LF, the arc was observed for both the high alloyed and carbon steel grades. Generally, OES slag composition analysis shows more prospects for the LF, because no solid charge material blocks the view to the arc, and the ladle treatment would greatly benefit from online slag composition analysis.

The different application possibilities of OES for electric steelmaking are versatile. The most beneficial aspect of OES is the capability of online data acquisition and analysis. If a clear line-of-sight to the electric arc can be arranged, OES spectrum analysis can be used to characterise the arc and estimate the slag composition during the furnace operation. The atomic and molecular optical emissions also contain information about plasma composition and the furnace atmosphere. However, if the arcs are visible only momentarily or not at all during the melting process, the radiative heat transfer and molten bath surface temperature can still be evaluated from the spectra. Yet the optical absorptions or emissions from the molecules in the furnace atmosphere or at the edges of the arc may contain information about the atmosphere composition. In the work of this thesis, OES has proven to be a potential candidate for an online process condition monitoring and slag composition analysis method for industrial EAFs and LFs.

References

[1] H.-J. Odenthal, A. Kemminger, F. Krause, L. Sankowski, N. Uebber, and N. Vogl, "Review on Modeling and Simulation of the Electric Arc Furnace (EAF)," *Steel Research International*, vol. 89, no. 1700098, 2018.

[2] T. Harada and H. Tanaka, "Future steelmaking model by direct reduction technologies," *ISIJ International*, vol. 51, pp. 1301–1307, 2011.

[3] M. Aula, A. Mäkinen, and T. Fabritius, "Analysis of Arc Emission Spectra of Stainless Steel Electric Arc Furnace Slag Affected by Fluctuating Arc Voltage," *Applied Spectroscopy*, vol. 68, no. 1, pp. 26–32, 2014.

[4] M. Aula, T. Demus, T. Echterhof, M. Huttula, and T. Fabritius, "On-line Analysis of Cr_2O_3 Content of the Slag in Pilot Scale EAF by Measuring Optical Emission Spectrum of Electric Arc," *ISIJ International*, vol. 57, pp. 478–486, 2017.

[5] M. Aula, A. Leppänen, J. Roininen, E.-P. Heikkinen, K. Vallo, T. Fabritius, and M. Huttula, "Characterization of Process Conditions in Industrial Stainless Steelmaking Electric Arc Furnace Using Optical Emission Spectrum Measurements," *Metallurgical and Materials Transactions B*, vol. 45, pp. 839–849, 2014.

[6] M. Aula, A. Mäkinen, A. Leppänen, M. Huttula, and T. Fabritius, "Optical emission analysis of slag surface conditions and furnace atmosphere during different process stages in electric arc furnace (EAF)," *ISIJ International*, vol. 55, no. 8, pp. 1702–1710, 2015.

[7] J. A. C. Broekaert, *Analytical Atomic Spectrometry with Flames and Plasmas.* Wiley-VCH Verlag GmbH Co. KGaA, 2002.

[8] B. Valeur, *Molecular Fluorescence: Principles and Applications.* Wiley-VCH Verlag GmbH, 2001.

[9] T. L. Meek, "An introduction to spectroscopy, atomic structure and chemical bonding," *Canoe Press, University Press of the West Indies*, 1998.

[10] A. Kramida, Y. Ralchenko, J. Reader, and N. Team, "NIST Atomic Spectra Database." [Online]. Available: `https://doi.org/10.18434/T4W30F`

[11] R. D. Cowan and G. H. Dieke, "Self-Absorption of Spectrum Lines," *Reviews of Modern Physics*, vol. 20, pp. 418–455, 1948.

[12] R. D. Cowan, *The Theory of Atomic Structure and Spectra.* University of California Press, 1981.

[13] B. Bowman and K. Krüger, *Arc Furnace Physics.* Düsseldorf, Germany: Verlag Stahleisen BmbH, 2009.

[14] M. C. Mantovani, C. Takanako, and P. M. Büchler, "EAF and secondary dust characterisation," *Ironmaking and Steelmaking*, vol. 31, no. 4, pp. 325–332, 2004.

[15] M. Alizadeh and M. Momeni, "The effect of the scrap/dri ratio on the specification of the eaf dust and its influence on mechanical properties of the concrete treated by its dust," *Construction and Building Materials*, vol. 112, pp. 1041–1045, 2016.

[16] M. C. D. Silva, A. M. Bernardes, C. P. Bergmann, J. A. S. Tenório, and D. C. R. Espinosa, "Characterisation of electric arc furnace dust generated during plain carbon steel production," *Ironmaking and Steelmaking*, vol. 35, no. 4, pp. 315–320, 2008.

[17] F. Opitz, P. Treffinger, and J. Wöllenstein, "Modeling of radiative heat transfer in an electric arc furnace," *Metallurgical and Materials Transactions B*, vol. 48, p. 3301–3315, 2017.

[18] J. Alexis, M. Ramirez, G. Trapaga, and P. Jönsson, "Modeling of a DC Electric Arc Furnace - Heat Transfer from the Arc," *ISIJ International*, vol. 40, p. 1089–1097, 2000.

[19] C. Aragón and J. A. Aguilera, "Characterization of laser induced plasmas by optical emission spectroscopy: A review of experiments and methods," *Spectrochimica Acta Part B*, vol. 63, p. 893–916, 2008.

[20] A. A. Ovsyannikov and M. F. Zhukov, *Plasma Diagnostics.* Cambridge: Cambridge International Science Publishers, 2000.

[21] G. Kühn and M. Kock, "Nonequilibrium phenomena and determination of plasma parameters in the hot core of the cathode region in free-burning arc discharges," *Physiscal Review E*, vol. 75, no. 016406, 2007.

[22] R. W. P. McWhirter, *Plasma Diagnostic Techniques.* New York: Academic Press, 1965.

[23] J. Madias, "Electric Furnace Steelmaking," *Treatise on Process Metallurgy*, vol. 3, pp. 271–300, 2014.

[24] T. Emi, "Steelmaking Technology for the Last 100 Years: Toward Highly Efficient Mass Production Systems for High Quality Steels," *ISIJ International*, vol. 55, pp. 36–66, 2015.

[25] S. S. Varanasi, V. M. R. More, M. B. V. Rao, S. R. Alli, A. K. Tangudu, and D. Santanu, "Recycling Ladle Furnace Slag as Flux in Steelmaking: A Review," *Journal of Sustainable Metallurgy*, vol. 5, pp. 449–462, 2019.

[26] L. Deng, X. Zhang, M. Zhang, and X. Jia, "Effect of CaF_2 on viscosity, structure and properties of CaO-Al_2O_3-MgO-SiO_2 slag glass ceramics," *Journal of Non-Crystalline Solids*, vol. 500, pp. 310–316, 2018.

[27] F. Shahbazian, "Experimental studies of the viscosities in the CaO-FeO-SiO_2-CaF_2 slags," *Scandinavian Journal of Metallurgy*, vol. 30, pp. 302–308, 2001.

[28] J. Bennett and K.-S. Kwong, "Thermodynamic studies of MgO saturated EAF slag," *Ironmaking and Steelmaking*, vol. 37, no. 7, pp. 529–535, 2010.

[29] A. P. Luz, A. G. T. Martinez, F. López, P. Bonadia, and V. C. Pandolfelli, "Slag foaming practice in the steelmaking process," *Ceramics International*, vol. 44, no. 8, pp. 8727–8741, 2018.

[30] R. D. Morales, L. G. Rubén, F. López, J. Camacho, and J. A. Romero, "The slag foaming practice in EAF and its influence on the steelmaking shop productivity," *ISIJ International*, vol. 35, pp. 1054–1062, 1995.

[31] H. Matsuura and R. J. Fruehan, "Slag foaming in an electric arc furnace," *ISIJ International*, vol. 49, no. 10, pp. 1530–1535, 2009.

[32] H. S. Kim, D. J. Min, and J. H. Park, "Foaming behavior of $CaO–SiO_2–FeO–MgO_{satd}–X(X=Al_2O_3$, MnO, P_2O_5, and CaF_2) slags at high temperatures," *ISIJ International*, vol. 41, pp. 317–324, 2001.

[33] D. Lotun and L. Pilon, "Physical modeling of slag foaming for various operating conditions and slag compositions," *ISIJ International*, vol. 45, pp. 835–840, 2005.

[34] S. Manocha and F. Ponchon, "Management of Lime in Steel," *Metals*, vol. 8, no. 686, 2018.

[35] E. Keskinkilic, A. Geveci, and Y. A. Topkaya, "Desulphurization characteristics of ladle furnace slags of a low sulphur steel," *Canadian Metallurgical Quarterly*, vol. 46, no. 4, pp. 391–396, 2007.

[36] J. H. Park, D. J. Ming, and H. S. Song, "The effect of CaF_2 on the viscosities and structures of CaO-SiO_2(-MgO)-CaF_2 slags," *Metallurgical and Materials Transactions B*, vol. 38, pp. 723–729, 2002.

[37] J. H. Park, K. Y. Ko, and T. S. Kim, "Influence of CaF_2 on the viscosity and structure of manganese ferroalloys smelting slags," *Metallurgical and Materials Transactions B*, vol. 46, pp. 741–748, 2015.

[38] L. V. Fisher and A. R. Barron, "The recycling and reuse of steelmaking slags — A review," *Resources, Conservation & Recycling*, vol. 146, pp. 244–255, 2019.

[39] Y. Liang, W. Li, and X. Wang, "Influence of Water Content on Mechanical Properties of Improved Clayey Soil Using Steel Slag," *Geotechnical and Geological Engineering*, vol. 31, p. 83–91, 2013.

[40] Y. Tabatabaei, K. S. Coley, G. A. Irons, and S. Sun, "Tracking Inclusions during Ladle Refining Using a Kinetic Model for the Compositions of Metal, Slag, and Inclusions," *Steel Research International*, vol. 90, no. 1900155, 2019.

[41] Y. Lin, B. Yan, T. Fabritius, and Q. Shu, "Immobilization of Chromium in Stainless Steel Slag Using Low Zinc Electric Arc Furnace Dusts," *Metallurgical and Materials Transactions B*, vol. 51, p. 763–775, 2020.

[42] Z. Huaiwei and H. Xin, "An overview for the utilization of wastes from stainless steel industries," *Resources, Conservation & Recycling*, vol. 55, pp. 745–754, 2011.

[43] I. Matino, V. Colla, and S. Baragiola, "Internal Slags Reuse in an Electric Steelmaking Route and Process Sustainability: Simulation of Different Scenarios Through the EIRES Monitoring Tool," *Waste Biomass Valorization*, vol. 9, no. 2481-2491, 2018.

[44] B. Lee and I. Sohn, "Review of innovative energy savings technology for the electric arc furnace," *The Journal of The Minerals, Metals & Materials Society*, vol. 66, pp. 1581–1594, 2014.

[45] Y. Jiang, T.-C. Ling, C. Shi, and S.-Y. Pan, "Characteristics of steel slags and their use in cement and concrete—A review," *Resources, Conservation & Recycling*, vol. 136, 2018.

[46] S. Carvalho, F. Vernilli, B. Almeida, M. Demarco, and S. Silva, "The recycling effect of BOF slag in the portland cement properties," *Resources, Conservation & Recycling*, vol. 127, pp. 216–220, 2017.

[47] H. Yi, G. Xu, H. Cheng, J. Wang, Y. Wang, and H. Chen, "An Overview of Utilization of Steel Slag," *Procedia Environmental Sciences*, vol. 16, pp. 791–801, 2012.

[48] M. Pasetto and N. Baldo, "Experimental evaluation of high performance base course and road base asphalt concrete with electric arc furnace steel slags," *Journal of Hazardous Materials*, vol. 181, no. 1-3, pp. 938–948, 2010.

[49] M. Pasetto and N. Baldo, "Experimental analysis of hydraulically bound mixtures made with waste foundry sand and steel slag," *Materials and Structures*, vol. 48, pp. 2489–2503, 2015.

[50] M. Pasetto and N. Baldo, "Recycling of waste aggregate in cement bound mixtures for road pavement bases and sub-bases," *Construction and Building Materials*, vol. 108, pp. 112–118, 2016.

[51] S. S. Harilal, C. V. Bindhu, R. C. Issac, V. P. N. Nampoori, and C. P. G. Vallabhan, "Electron density and temperature measurements in a laser produced carbon plasma," *Journal of Applied Physics*, vol. 82, pp. 2140–2146, 1997.

[52] N. M. Shaikh, B. Rashid, H. Hafeez, Y. Jamil, and M. A. Baig, "Measurement of electron density and temperature of a laser-induced zinc plasma," *Journal of Physics D: Applied Physics*, vol. 39, no. 7, pp. 1384–1391, 2006.

[53] N. M. Shaikh, S. Hafeez, B. Rashid, and M. A. Baig, "Spectroscopic studies of laser induced aluminum plasma using fundamental, second and third harmonics of a Nd:YAG laser," *European Physical Journal D*, vol. 44, pp. 371–379, 2007.

[54] S. Paik and H. D. Nguyen, "Numerical modeling of multiphase plasma/soil flow and heat transfer in an electric arc furnace," *International Journal of Heat and Mass Transfer*, vol. 38, pp. 1161–1171, 1995.

[55] M. Guo, D. Durinck, P. T. Jones, G. Heylen, R. Hendrickx, R. Baeten, B. Blanpain, and P. Wollants, "EAF Stainless Steel Refining - Part I: Observational Study on Chromium Recovery in an Eccentric Bottom Tapping Furnace and a Spout Tapping Furnace," *Steel Research International*, vol. 78, pp. 117–124, 2007.

[56] D. Durinck, P. T. Jones, M. Guo, F. Verhaeghe, G. Heylen, R. Hendrickx, R. Baeten, B. Blanpain, and P. Wollants, "EAF Stainless Steel Refining - Part II: Microstructural Slag Evolution and its Implications for Slag Foaming and Chromium Recovery," *Steel Research International*, vol. 78, pp. 125–135, 2007.

[57] X. Hao, X.-H. Wang, and W.-J. Wang, "Effect of slag composition on desulfurization and inclusion modification during ladle furnace refining," *Metallurgical Research & Technology*, vol. 111, pp. 239–245, 2014.

[58] C. Liu, F. Huang, and X. Wang, "The effect of refining slag and refractory on inclusion transformation in extra low oxygen steels," *Metallurgical and Materials Transactions B*, vol. 47, pp. 999–1009, 2016.

[59] J.-F. Xu, K.-P. Wang, Y. Wang, Z.-D. Qu, and X.-K. Tu, "Effects of ferrosilicon alloy, Si content of steel, and slag basicity on compositions of inclusions during ladle furnace refining of Al-killed steel," *Journal of Iron and Steel Research International*, 2020. [Online]. Available: `https://doi.org/10.1007/s42243-020-00384-2`

[60] F. Huang, C. Liu, N. Maruoka, and S.-Y. Kitamura, "Dissolution behaviour of MgO based refractories in $CaO–Al_2O_3–SiO_2$ slag," *Ironmaking & Steelmaking*, vol. 42, pp. 553–560, 2015.

[61] A. Conejo, R. Lule, F. Lopéz, and R. Rodriguez, "Recycling MgO-C refractory in electric arc furnaces," *Resources, Conservation & Recycling*, vol. 49, pp. 14–31, 2006.

[62] R. Miotk, M. Jasinski, and J. Mizeraczyk, "Optical Emission Spectroscopy of Microwave (915 MHz) Plasma in Atmospheric Pressure Nitrogen with Addition of Ethanol Vapour," *Acta Physica Polonica A*, vol. 125, pp. 1329–1331, 2014.

[63] A. Firsov, K. V. Savelkin, D. A. Yarantsev, and B. Leonov, "Plasma-enhanced mixing and flameholding in supersonic flow," *Philosophical Transactions of the Royal Society A*, vol. 373, no. 20140337, 2015.

[64] P. Jamroz and W. Zyrnicki, "Study of the dc and 100 khz glow discharges in acetylene-nitrogen mixture by means of optical emission spectroscopy," *The European Physical Journal: Applied Physics*, vol. 19, pp. 201–209, 2002.

[65] M. Dong, J. Lu, S. Yao, Z. Zhong, J. Li, J. Li, and W. Lu, "Experimental study on the characteristics of molecular emission spectroscopy for the analysis of solid materials containing C and N," *Optics Express*, vol. 19, pp. 17 021–17 029, 2011.

[66] J. J. Camacho, L. Díaz, M. Santos, D. Reyman, and J. M. L. Poyato, "Optical emission spectroscopic study of plasma plumes generated by IR CO_2 pulsed laser on carbon targets," *Journal of Physics D: Applied Physics*, vol. 41, no. 105201, 2008.

[67] P. Dagaut, P. Glarborg, and M. U. Alzueta, "The oxidation of hydrogen cyanide and related chemistry," *Progress in Energy and Combustion Science*, vol. 34, pp. 1–46, 2008.

[68] L. R. Thorne, M. C. Branch, D. W. Chandler, R. J. Kee, and J. A. Miller, "Hydrocarbon/nitric oxide interactions in low-pressure flames," *Symposium (International) on Combustion*, vol. 21, pp. 965–977, 1988.

[69] C. Y. Wang, S. Zhang, and Q. S. Li, "Ab initio study of rate constants of the reaction: HCN + OH $\rightarrow$ CN + H_2O," *Theoretical Chemistry Accounts*, vol. 108, pp. 341–346, 2002.

[70] M. Gaft, L. Nagli, N. Eliezer, Y. Groisman, and O. Forni, "Elemental analysis of halogens using molecular emission by laser-induced breakdown spectroscopy in air," *Spectrochimica Acta Part B: Atomic Spectroscopy*, vol. 98, pp. 39–47, 2014.

[71] A. Mäkinen, J. Niskanen, H. Tikkala, and H. Aksela, "Optical emission from a small scale model electric arc furnace in 250–600 nm region," *Review of Scientific Instruments*, vol. 84, no. 043111, 2013.

Original papers

I. Pauna H, Willms T, Aula M, Echterhof T, Huttula M, Fabritius T (2019) Pilot-scale AC electric arc furnace plasma characterization. Plasma Research Express. 1(3): 035007.

II. Pauna H, Willms T, Aula M, Echterhof T, Huttula M, Fabritius T (2020) Electric arc length-voltage and conductivity characteristics in a pilot-scale AC electric arc furnace. Metallurgical and Materials Transactions B. 51(4): 1646-1655.

III. Pauna H, Aula M, Seehausen J, Klung J-S, Huttula M, Fabritius T (2020) Optical emission spectroscopy as an on-line analysis method in industrial electric arc furnaces. Steel Research International. 2000051. Article published online https://doi.org/10.1002/srin.202000051.

IV. Pauna H, Aula M, Seehausen J, Klung J-S, Huttula M, Fabritius T (2020) Industrial Ladle Furnace Slag Composition Analysis with Optical Emissions from the Arc. ISIJ International. Advance online publication https://doi.org/10.2355/isijinternational.ISIJINT-2019-676.

Original publications are not included in the electronic version of the dissertation.